



# Fault-tolerant control for four-wheel independent actuated electric vehicle using feedback linearization and cooperative game theory

Bohan Zhang, Shaobo Lu \*

State Key Laboratory of Mechanical Transmission, School of Automotive Engineering, Chongqing University, Chongqing 400044, PR China



## ARTICLE INFO

### Keywords:

Fault-tolerant control  
Lateral stability  
Cooperative game  
Nonlinear control  
Feedback linearization

## ABSTRACT

This paper presents a novel fault-tolerant control (FTC) approach based on the cooperative game to guarantee the stability of four-wheel independent drive electric vehicles, in which four different players are modeled and interacted to find a solution to the FTC problem. First, a feedback linearization approach is employed to handle the nonlinearities in the system. Then, to study the interaction among actuators in an actuator failure scenario, the FTC problem can be viewed as a cooperative game so that its four players, namely the four in-wheel motors can cooperate to provide more stability of the vehicle. The distributed model predictive control theory is adopted as a general framework, the Pareto strategies among the players are derived using an interactive model based on a convex iterative method. Furthermore, the conditions that guarantee the practical stability of the closed-loop system are provided. The intrinsic differences between the cooperative game and noncooperative game are investigated via a numerical simulation. The effectiveness and real-time of the proposed control strategy are verified in a real-time hardware-in-the-loop test, and the results prove that the control strategy can effectively guarantee the stability of the vehicle in various actuator failure scenarios.

## 1. Introduction

The four-wheel independent drive electric vehicles (4WID-EVs) have been recognized as a breakthrough concept that will have a major impact on future vehicle design, as their chassis structure has some advantages, such as actuation flexibility, fast torque response and all-wheel-independent-control (Shuai, Zhang, Wang, Li, & Ouyang, 2014). Many researchers are, therefore, vigorously researching and developing advanced stability control for this redundant system, such as torque distribution control and steer-by-wire (SBW) control (Erlien, Fujita, & Gerdes, 2016; Huang, Naghdy, & Du, 2019b; Joa, Yi, Sohn, & Bae, 2018; Zhang & Wang, 2016). However, these technologies improve not only the driving flexibility and active safety but also the probability of the actuator faults due to the significantly increased system complexity and the number of actuators. It implies that the fault-tolerant control (FTC) has a positive impact on vehicle safety.

To guarantee the stability of the faulty vehicle, a large variety of methods are applied in FTC, such as the optimal method (Zhang, Liu, Zhou, & Zhao, 2018), robust control method (Guo & Chen, 2019; Sakthivel, Mohanapriya, Kaviarasan, Ren, & Anthoni, 2020), linear parameter-varying (LPV) control (Mihaly, Gaspar, & Nemeth, 2017), sliding mode control (Chen et al., 2019; Huang, Naghdy, & Du, 2019a; Zhang, Liu, Zhou, & Zhao, 2018). Sakthivel, Mohanapriya, Ahn, and Selvaraj (2018) studied a probability-dependent FTC state feedback controller that involves a fuzzy rule-based state estimator. Besides,

nonlinear FTC has also attracted a lot of attention. Wang and Wang (2013) proposed a passive FTC based on state feedback for a multiple-input-multiple-output (MIMO) nonlinear system. Hu, Wang, Yan, and Karimi (2016) developed a nonlinear feedback approach to realize the path-following control during the complete failure of the active front steering (AFS). Wang, Gao, Li and Chen (2019), Wang, Zong, Li and Chen (2019) and Wang, Yu, Yuan, and Chen (2018) reported a triple-step nonlinear control approach to deal with the motion control of the faulty vehicle. The above researches have applied the centralized control methods in FTC. However, the theoretical framework of interaction among subsystems of distributed architecture is lacking studied.

Differential game theory is a theoretical framework that provides an opportunity to study the interaction and cooperation among different agents (Maestre, de la Pena, & Camacho, 2011). In recent years, the use of differential game theory to maintain vehicle stability has been reported by many researchers. This method permits the quadratic cost functions of the actuator to be taken as players and then derives the equilibrium solution based on game theory. The mode of game can be either noncooperative or cooperative depending on the players' attitude toward themselves interest or collective interest (Na & Cole, 2015). Tamaddoni, Taheri, and Ahmadian (2011) first reported a Nash equilibrium solution for the driver and the direct yaw moment controller (DYC) based on linear quadratic (LQ) noncooperative differential game. Na and Cole (2015) used a Nash noncooperative game method to solve

\* Corresponding author.

E-mail address: [lsb@cqu.edu.cn](mailto:lsb@cqu.edu.cn) (S. Lu).

the conflict between the steering of the driver and the active collision avoidance system. A noncooperative Stackelberg game is also widely used to deals with the interaction between subsystems, such as the DYC and AFS (Zhao, Lu, & Zhang, 2019), the AFS and active rear steering (ARS) (Ji et al., 2018), and the driver and intelligent electric power steering system (Ji, Yang, Na, Lv, & Liu, 2019).

On the other hand, the development of distributed model predictive control (DMPC) based cooperative game schemes has received increasing attention, where players share global information to improve closed-loop performance and fault-tolerance (Maestre et al., 2011). Na and Cole (2015, 2019) have also studied the application of DMPC-based cooperative game in driver–vehicle interaction. Moreover, they point out that the strategies derived from the DMPC-based cooperative game are in the sense of Pareto equilibrium. Therefore, the DMPC-based cooperative game is a promising research direction in FTC. However, to the best of the authors' knowledge, the cooperative game of  $n$ -players is rarely discussed in the field of FTC.

Another issue associated with the FTC of the 4WID-EVs is the actuator failures will cause the vehicle to travel in critical conditions where tire forces are approaching to or at the limit of road adhesion, the vehicle side-slip angle grows and the dynamic behavior of the vehicle will be nonlinear (Mirzaei, Alizadeh, Eslamian, & Azadi, 2008). In the past few decades, differential geometry has proved to be an effective approach to analysis and design of nonlinear control systems, different from the traditional approximate linearization methods, an affine nonlinear system can be exact linearized by the feedback linearization method without ignoring any higher-order terms (Yang, Feng, & Zhang, 2017). Inspired by this methodology, the feedback linearization technique is used to linearize the MIMO nonlinear vehicle model in this work.

This paper focuses on the development of a double-layer hierarchical FTC strategy that can guarantee the stability of 4WID-EVs and deal with the system's nonlinear characteristics and interaction among actuators. The main contributions are as follows: First, a double-layer hierarchical framework is proposed to treat the nonlinear characteristics and the cooperation among the actuators of the faulty vehicle simultaneously. The layering of the controller is achieved by analyzing the control effect of different actuators. Second, the nonlinear characteristics of the faulty vehicle are handled by the input–output feedback linearization method. Third, in the lower-level controller, the interactive paradigm among the healthy actuators is achieved based on the cooperative game theory. The actuators are modeled as the players in the game, and the Pareto strategies are derived based on DMPC.

The remainder of this paper is as follows: The establishment of a nonlinear vehicle model with actuator failures is described in Section 2, the idea of hierarchical based on control efforts of different actuators is introduced. In Section 3, the feedback linearization method adopts in the upper-level controller is described. The design of the cooperative game based lower-level controller is introduced in Section 4. In Section 5, a numerical simulation and a real-time hardware-in-the-loop (RT-HIL) test are performed on the designed algorithm, where the results are exhibited and analyzed. Finally, Section 6 concludes this research.

## 2. Modeling of vehicle and actuator fault

### 2.1. Vehicle dynamic modeling

In this paper, four in-wheel motors and front steering motor are the actuators considered, and the vehicle is assumed to be equipped with SBW technology. The vehicle dynamics model shown in Fig. 1 is modeled with an appropriate degree of fidelity (Wang, Zong et al., 2019). This simplified model capturing the essential features of the vehicle system is employed in the control method design.

The vehicle equations of motion in the longitudinal, lateral, and yaw can be expressed as follows:

$$\left\{ \begin{array}{l} \dot{v}_x = v_y \omega + \frac{\cos \delta_f}{m} F_{xfl} + \frac{\cos \delta_f}{m} F_{xfr} + \frac{1}{m} F_{xrl} + \frac{1}{m} F_{xrr} \\ \quad + \frac{\sin \delta_f}{m} F_{yfl} + \frac{\sin \delta_f}{m} F_{yfr} \\ \dot{v}_y = -v_x \omega + \frac{\sin \delta_f}{m} F_{xfl} + \frac{\sin \delta_f}{m} F_{xfr} + \frac{\cos \delta_f}{m} F_{yfl} + \frac{\cos \delta_f}{m} F_{yfr} \\ \quad + \frac{1}{m} F_{yrl} + \frac{1}{m} F_{yrr} \\ \dot{\omega} = \frac{a \sin \delta_f - t_f \cos \delta_f}{I_z} F_{xfl} + \frac{a \sin \delta_f + t_f \cos \delta_f}{I_z} F_{xfr} \\ \quad - \frac{t_r}{I_z} F_{xrl} + \frac{t_r}{I_z} F_{xrr} \\ \quad + \frac{t_f \sin \delta_f + a \cos \delta_f}{I_z} F_{yfl} + \frac{-t_f \sin \delta_f + a \cos \delta_f}{I_z} F_{yfr} - \frac{b}{I_z} F_{yrl} \\ \quad - \frac{b}{I_z} F_{yrr} \end{array} \right. \quad (1)$$

where  $m$  is the vehicle total mass,  $F_{xij}$  and  $F_{yij}$  are the longitudinal and the lateral tire forces of the wheel  $ij$ , respectively,  $ij := \{fl, fr, rl, rr\}$  indicate the front-left, front-right, rear-left and rear-right wheel, respectively,  $t_f$  and  $t_r$  are the half-track width of the front and rear axle, respectively,  $\delta_f$  is the steering angle of the front wheel which is the superposition of the steering angle provided by the driver and AFS,  $v_x$  and  $v_y$  are the longitudinal and lateral velocities,  $\omega$  is the yaw rate,  $a$  and  $b$  are the distance from the center of gravity (CG) to the front and rear axle, respectively,  $I_z$  is the vehicle yaw moment of inertia. In this paper, assuming that the above vehicle state parameters can be directly measured or estimated based on advanced technology, e.g. Unscented Kalman Filter (UKF) (Chen, Zhang, Chen and Fu, 2019).

Considering the rolling resistance of the tire, the rotational dynamics of each wheel can be expressed as follows:

$$I_w \dot{\omega}_{w,ij} = T_{ij} - R_{eff} (F_{xij} + F_{ij,roll}) \quad (2)$$

where  $I_w$  is the tire moment of inertia,  $\omega_{w,ij}$  is the tire rotational speed,  $T_{ij}$  is the motor torque,  $R_{eff}$  is the tire effective radius,  $F_{ij,roll}$  denotes the tire rolling resistance, which can be expressed by the following empirical formula (Wang & Wang, 2013):

$$F_{i,roll} = F_{zij} (e_1 + e_2 v_x^2) \quad (3)$$

where  $e_1$  and  $e_2$  are the rolling resistance coefficients in the order of  $4 \times 10^{-2}$  and  $2.5 \times 10^{-6}$ , respectively,  $F_{zij}$  denotes the vertical tire force and can be estimated by the longitudinal and lateral accelerations as:

$$\left\{ \begin{array}{l} F_{zfl}, F_{zfr} = \frac{m}{2L} \left( g b - a_x h \mp \frac{a_y b h}{t_f} \right) \\ F_{zrl}, F_{zrr} = \frac{m}{2L} \left( g a - a_x h \mp \frac{a_y a h}{t_r} \right) \end{array} \right. \quad (4)$$

where  $g$  denotes the gravitational acceleration,  $a_x$  and  $a_y$  are the longitudinal and lateral acceleration, respectively,  $L$  is the wheelbase and  $L = a + b$ ,  $h$  is the height of the vehicle's CG.

On the assumption of the small side-slip angles, the front and rear lateral tire forces can be modeled approximately as:

$$F_{yfl}, F_{yfr} = c_f \alpha_f, F_{yrl}, F_{yrr} = c_r \alpha_r \quad (5)$$

where  $c_f$  and  $c_r$  are the cornering stiffness of the front and rear tires, respectively,  $\alpha_f$  and  $\alpha_r$  denote the front and rear tire slip angle, respectively, that can be expressed as:

$$\left\{ \begin{array}{l} \alpha_f = \delta_f - \arctan \left( \frac{v_y + a\omega}{v_x} \right) \\ \alpha_r = \arctan \left( \frac{b\omega - v_y}{v_x} \right) \end{array} \right. \quad (6)$$

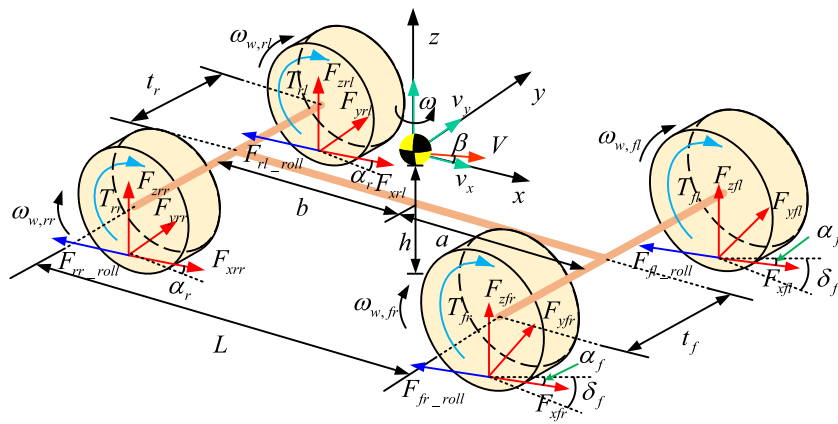


Fig. 1. Vehicle dynamic model.

## 2.2. Actuator faults modeling

The effect of actuator faults on the vehicle system is represented by the actuator fault modeling. In this study, these three most common faults of the in-wheel motor, i.e., additive fault, stuck-at-fixed-level fault, and the loss-of-effectiveness are considered (Zhang et al., 2016). The generalized form of actuator faults is defined as follows:

$$T_{ij} = \epsilon_{ij} T_{d,ij} + \Delta T_{ij} \begin{cases} \epsilon_{ij} = 1 \& \Delta T_{ij} = 0 & \text{Healthy} \\ \epsilon_{ij} = 1 \& \Delta T_{ij} = \text{const.} & \text{Additive fault} \\ \epsilon_{ij} = 0 \& \Delta T_{ij} = \text{const.} & \text{Stuck - at - fixed - level fault} \\ \epsilon_{ij} \in (0, 1) \& \Delta T_{ij} = 0 & \text{Loss - of - effectiveness} \end{cases} \quad (7)$$

where  $T_{ij}$  is the actual motor torque,  $\epsilon_{ij}$  denotes the loss-of-effectiveness gain,  $T_{d,ij}$  is the desired motor torque,  $\Delta T_{ij}$  represents the extra torque caused by the fault, and it is assumed to be bounded. It is assumed in this study that the actuator failure information can be obtained by the fault diagnosis and detection method suggested by Wang and Wang (2011).

Considering Eqs. (2) and (5)–(7), Eq. (1) can be rewritten as:

$$\dot{v}_x = f_1(\mathbf{x}) + \frac{1}{R_{eff}} \mathbf{B}_{T,1} \mathbf{E} \mathbf{T}_d + \mathbf{B}_{T,1} \hat{\mathbf{F}} + \frac{2c_f \sin \delta_f}{m} \delta_f \quad (8)$$

$$\dot{v}_y = f_2(\mathbf{x}) + \frac{1}{R_{eff}} \mathbf{B}_{T,2} \mathbf{E} \mathbf{T}_d + \mathbf{B}_{T,2} \hat{\mathbf{F}} + \frac{2c_f \cos \delta_f}{m} \delta_f \quad (9)$$

$$\dot{\omega} = f_3(\mathbf{x}) + \frac{1}{R_{eff}} \mathbf{B}_{T,3} \mathbf{E} \mathbf{T}_d + \mathbf{B}_{T,3} \hat{\mathbf{F}} + \frac{2ac_f \cos \delta_f}{I_z} \delta_f \quad (10)$$

where  $\mathbf{B}_{T,i}$  is the  $i$ th row of the matrix  $\mathbf{B}_T$ , and

$$\mathbf{B}_T = \begin{bmatrix} \frac{\cos \delta_f}{m} & \frac{\cos \delta_f}{m} & \frac{1}{m} & \frac{1}{m} \\ \frac{\sin \delta_f}{m} & \frac{\sin \delta_f}{m} & 0 & 0 \\ \frac{a \sin \delta_f - t_f \cos \delta_f}{I_z} & \frac{a \sin \delta_f + t_f \cos \delta_f}{I_z} & -\frac{t_r}{I_z} & \frac{t_r}{I_z} \end{bmatrix}, \quad (3 \times 4) . 4 \times 1$$

$$\mathbf{x} = [v_x \ v_y \ \omega]^T,$$

$$f_1(\mathbf{x}) = v_y \omega - \frac{2c_f \sin \delta}{m} \left( \arctan \left( \frac{v_y + a\omega}{v_x} \right) \right),$$

$$f_2(\mathbf{x}) = -v_x \omega - \frac{2c_f \cos \delta}{m} \arctan \left( \frac{v_y + a\omega}{v_x} \right) + \frac{2c_r}{m} \arctan \left( \frac{b\omega - v_y}{v_x} \right)$$

$$f_3(\mathbf{x}) = -\frac{2ac_f \cos \delta}{I_z} \arctan \left( \frac{v_y + a\omega}{v_x} \right) - \frac{2bc_r}{I_z} \arctan \left( \frac{b\omega - v_y}{v_x} \right),$$

$M_x \text{ (Nm)}$

$\omega_x \text{ (rad/s)}$

$$\mathbf{T}_d = [T_{d,fl} \ T_{d,fr} \ T_{d,rl} \ T_{d,rr}]^T, \hat{\mathbf{F}} = [\hat{F}_{fl} \ \hat{F}_{fr} \ \hat{F}_{rl} \ \hat{F}_{rr}]^T,$$

$$\hat{F}_{ij} = \frac{\Delta T_{ij}}{R_{eff}} - \frac{I_w \dot{\omega}_{w,ij}}{R_{eff}} + F_{ij\_roll},$$

$$\mathbf{E} = \text{diag} [\epsilon_{fl} \ \epsilon_{fr} \ \epsilon_{rl} \ \epsilon_{rr}].$$

W  
δ  
tanja Park Hall

The desired motor torques are provided by the in-wheel motors, and the front steering angle is affected by AFS. Considering that the two types of actuators affect the longitudinal and lateral tire forces of the vehicle, respectively, Eqs. (8)–(10) can be easily rewritten as two groups of equations.

$$\begin{cases} \dot{v}_y = f_2(\mathbf{x}) + \frac{1}{R_{eff}} \mathbf{B}_{T,2} \mathbf{E} \mathbf{T}_d + \mathbf{B}_{T,2} \hat{\mathbf{F}} + \frac{2c_f \cos \delta_f}{m} \delta_f \\ \dot{\omega} = f_3(\mathbf{x}) + \frac{2ac_f \cos \delta_f}{I_z} \delta_f + \frac{M_x}{I_z} \end{cases} \quad (11)$$

$$\begin{cases} \dot{v}_x = f_1(\mathbf{x}) + \frac{1}{R_{eff}} \mathbf{B}_{T,1} \mathbf{E} \mathbf{T}_d + \mathbf{B}_{T,1} \hat{\mathbf{F}} + \frac{2c_f \sin \delta_f}{m} \delta_f \\ \dot{\omega}_x = \frac{M_x}{I_z} = \frac{1}{R_{eff}} \mathbf{B}_{T,3} \mathbf{E} \mathbf{T}_d + \mathbf{B}_{T,3} \hat{\mathbf{F}} \end{cases} \quad (12)$$

where  $M_x$  and  $\omega_x$  denote the virtual additional yaw moment and virtual yaw rate, respectively, which are related to the longitudinal tire forces.

It can be noted that simultaneous Eqs. (11) and (12) are equivalent to Eqs. (8)–(10). The design of the hierarchical controller is based on Eqs. (11) and (12) which corresponds to the upper-level controller and the lower-level controller, respectively.

### 3. Feedback linearization based upper nonlinear control strategy

The structure of the control system is shown in Fig. 2. This architecture includes a driver-vehicle loop, a reference model, a fault detection system and a hierarchical controller. The desired states are generated via the reference model based on the single-track model and envelop boundaries. The fault detection system can diagnose the faults of in-wheel motors, and whose design is not within the scope of this paper and can be found in the appropriate literature (Wang & Wang, 2011).

As shown in Fig. 2, the control sequence of the upper-level controller is obtained according to the feedback control law, which includes the AFS angle and the virtual additional yaw moment  $M_x$ . The virtual additional yaw moment is considered as a desired value of the lower-level controller.

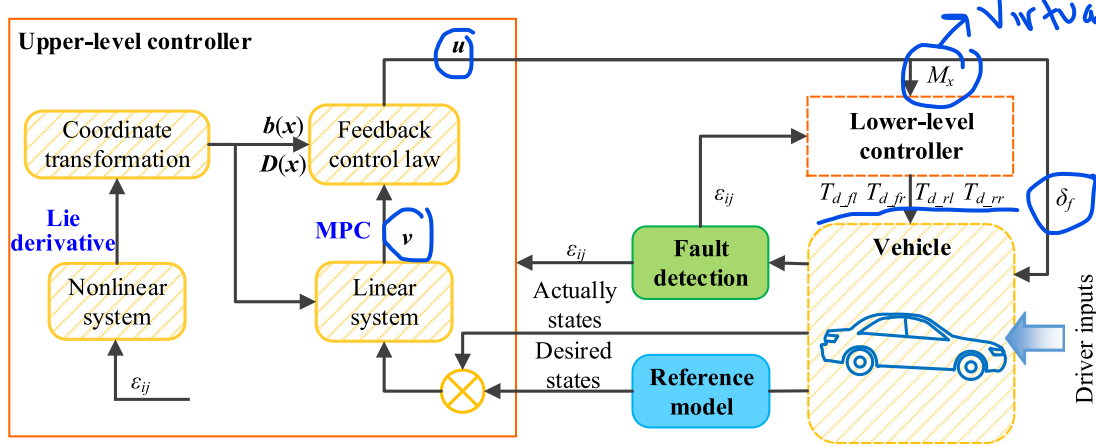


Fig. 2. Block diagram of the control scheme.

### 3.1. Exact linearization of nonlinear vehicle system

The upper-level controller is based on the system (11) which has a nonlinear feature caused by lateral tire forces. The given nonlinear vehicle system can be controlled through the input-output feedback linearization method that converts the nonlinear system into a controllable linear system via diffeomorphism. The implementation of feedback linearization on the upper-level controller can be described through the following steps:

Step 1: Extend the nonlinear vehicle model and select output functions.

In order to avoid zero dynamics and facilitate feedback linearization, it is necessary to build a square MIMO nonlinear system, that is, system with as many inputs as outputs. Therefore, the control channel for lateral displacement  $S_{Lat}$  is added to Eq. (11), and the output function  $h(\mathbf{x}^{up})$  should be selected. Thereby, the nonlinear state-space realization form of the affine system is defined as follows:

$$\begin{cases} \dot{\mathbf{x}}^{up} = \hat{f}(\mathbf{x}^{up}) + \hat{g}(\mathbf{x}^{up})\mathbf{u} \\ \mathbf{y} = \mathbf{C}\mathbf{x}^{up} = h(\mathbf{x}^{up}) \end{cases} \quad (13)$$

where

$$\begin{aligned} \mathbf{x}^{up} &= [v_y \quad \omega \quad S_{Lat}]^T, \quad h(\mathbf{x}^{up}) = [\omega \quad S_{Lat}]^T, \\ \hat{f}(\mathbf{x}^{up}) &= [\hat{f}_1(\mathbf{x}^{up}) \quad \hat{f}_2(\mathbf{x}^{up}) \quad \hat{f}_3(\mathbf{x}^{up})]^T, \end{aligned}$$

$$\mathbf{C} = \begin{bmatrix} 0 & 1 & 0 \\ 0 & 0 & 1 \end{bmatrix}, \quad \mathbf{u} = [\delta_f \quad M_x]^T$$

$$\hat{g}(\mathbf{x}^{up}) = \begin{bmatrix} \frac{2c_f \cos \delta_f}{m} & 0 \\ \frac{2ac_f \cos \delta_f}{I_z} & \frac{1}{I_z} \\ 0 & 0 \end{bmatrix}, \quad \begin{cases} \hat{f}_1(\mathbf{x}^{up}) = f_2(\mathbf{x}^{up}) \\ \hat{f}_2(\mathbf{x}^{up}) = f_3(\mathbf{x}^{up}) \\ \hat{f}_3(\mathbf{x}^{up}) = v_y + v_x \psi \end{cases} + \frac{1}{R_{eff}} \mathbf{B}_{T,2} \mathbf{E} \mathbf{T}_d + \mathbf{B}_{T,2} \hat{\mathbf{F}},$$

and  $\psi$  denotes the heading angle.

The main idea of feedback linearization for MIMO nonlinear systems are as follows, start by differentiating the  $i$ th output  $y_i$  of the system (13), and define  $r_i$  to be the smallest integer such that at least one of the inputs appears in  $y_i^{(r_i)}$ , the follows can be obtained (Shankar, 1999):

$$y_i^{(r_i)} = L_{\hat{f}}^{r_i} h_i + \sum_{j=1}^m L_{\hat{g}_j} L_{\hat{f}}^{r_i-1} h_j u_j \quad (14)$$

with at least one of the  $L_{\hat{g}_j} L_{\hat{f}}^{r_i-1} h_j \neq 0$ , for some  $x$ ,  $L_{\hat{f}}^{r_i}(\cdot)$  is the notation of Lie derivative, and its calculation method can be found in related literature (Mahmud, Pota, & Hossain, 2012).  $m$  indicates the number of system outputs.

#### Step 2: Calculating the relative degree and decoupling matrix.

In this step, the relative degree of the system needs to be calculated according to Definition 1.

**Definition 1 (Relative Degree Isidori, 1995).** If the following conditions are satisfied for all  $\mathbf{x} \in \mathbb{R}^n$  in the neighborhood of  $\mathbf{x}_0$ :

- (1)  $L_{\hat{g}_j} L_{\hat{f}}^k h_i \equiv 0$ ,  $(1 \leq i \leq m, 1 \leq j \leq m, 0 \leq k < r_i - 1)$ ;
- (2) The square decoupling matrix

$$D(\mathbf{x}_0) = \begin{bmatrix} L_{\hat{g}_1} L_{\hat{f}}^{r_1-1} h_1 & \dots & L_{\hat{g}_m} L_{\hat{f}}^{r_1-1} h_1 \\ \vdots & \ddots & \vdots \\ L_{\hat{g}_1} L_{\hat{f}}^{r_m-1} h_m & \dots & L_{\hat{g}_m} L_{\hat{f}}^{r_m-1} h_m \end{bmatrix} \quad (15)$$

is nonsingular. The nonlinear system is then said to have a vector relative degree  $r = \sum_{i=1}^m r_i$ .

The relative degree of the system (13) can be calculated as follows.

First, calculating the Lie derivative of  $h_1$ :

$$L_{\hat{g}_1} h_1 = \frac{2ac_f \cos \delta_f}{I_z} \neq 0 \text{ and } L_{\hat{g}_2} h_1 = \frac{1}{I_z} \neq 0;$$

Second, calculating the Lie derivative of  $h_2$ :

$$\begin{aligned} L_{\hat{g}_1} h_2 &= 0, \quad L_{\hat{g}_2} h_2 = 0, \quad L_{\hat{g}_1} L_{\hat{f}} h_2 = \frac{\partial(L_{\hat{f}} h_2)}{\partial x} \hat{g}_1(\mathbf{x}^{up}) = \frac{2c_f \cos \delta_f}{m} \neq 0, \\ L_{\hat{g}_2} L_{\hat{f}} h_2 &= \frac{\partial(L_{\hat{f}} h_2)}{\partial x} \hat{g}_2(\mathbf{x}^{up}) = 0. \end{aligned}$$

The first clause of Definition 1 is satisfied, and  $r_1 = 1, r_2 = 2$ . The relative degree of the system is  $r = r_1 + r_2 = 1 + 2 = 3$ .

The state-space exact linearization problem is solvable if and only if the system has some vector relative degree  $\{r_1, \dots, r_m\}$  at  $\mathbf{x}_0$  and  $r = \text{length}(\mathbf{x})$  (Isidori, 1995). Obviously, the nonlinear system (13) satisfies this condition.

Step 3: Coordinate transformation and formulate a linearized system model.

Following the diffeomorphism theory introduced by Shankar (1999), the original nonlinear system can be transformed into a controllable linear system through coordinate transformation by choosing:

$$\mathbf{z} = \phi(\mathbf{x}^{up}) = \begin{cases} h_1 \\ h_2 \\ L_{\hat{f}} h_2 = v_y + v_x \psi \end{cases} \quad (16)$$

and

$$\dot{\mathbf{z}} = \begin{cases} h_1 = v_1 \\ h_2 = \dot{S}_{Lat} = v_y + v_x \psi = z_3 \\ \frac{\partial(L_{\hat{f}} h_2)}{\partial \mathbf{x}^{up}} \frac{dx^{up}}{dt} = L_{\hat{f}}^2 h_2 + L_{\hat{g}} L_{\hat{f}} h_2 = v_2 \end{cases} \quad (17)$$

Therefore, the differential equation shown follows can be obtained:

$$\begin{cases} \dot{\mathbf{z}} = \mathbf{A}_c^{up} \mathbf{z} + \mathbf{B}_c^{up} \mathbf{v} \\ \mathbf{y}^{up} = \mathbf{C}^{up} \mathbf{z} \end{cases} \quad (18)$$

where  $\mathbf{v}$  is the virtual control vector of the linear system.

$$\mathbf{y}^{up} = [\omega \quad S_{Lat} + \dot{S}_{Lat}]^T, \quad \mathbf{A}_c^{up} = \begin{bmatrix} 0 & 0 & 0 \\ 0 & 0 & 1 \\ 0 & 0 & 0 \end{bmatrix}, \quad \mathbf{B}_c^{up} = \begin{bmatrix} 1 & 0 \\ 0 & 0 \\ 0 & 1 \end{bmatrix},$$

$$\mathbf{C}^{up} = \begin{bmatrix} 1 & 0 & 0 \\ 0 & 1 & 1 \end{bmatrix}$$

Step 4: Solving the virtual control sequence  $\mathbf{v}$  based on MPC and obtaining the actual control sequence  $\mathbf{u}$  of the upper controller according to the feedback control law,

$$\mathbf{u} = \mathbf{D}^{-1}(\mathbf{x}^{up})(-\mathbf{b}(\mathbf{x}^{up}) + \mathbf{v}) \quad (19)$$

$$\text{where } \mathbf{b}(\mathbf{x}) = [L_f^{r_1} h_1 \dots L_f^{r_m} h_m]^T.$$

The design of the MPC controller will be introduced in the next subsection.

### 3.2. MPC controller design

For the controller digital design, discretization Eq. (18) using the Euler method (Wang, Zong et al., 2019).

$$\begin{cases} \mathbf{z}(k+1) = \mathbf{A}_d^{up} \mathbf{z}(k) + \mathbf{B}_d^{up} \mathbf{v}(k) \\ \mathbf{y}^{up}(k) = \mathbf{C}^{up} \mathbf{z}(k) \end{cases} \quad (20)$$

where  $\mathbf{A}_d^{up} = \mathbf{I} + \mathbf{A}_c^{up} T_s$ ,  $\mathbf{B}_d^{up} = \mathbf{B}_c^{up} T_s$ , and  $T_s$  is a small sampling interval.

The prediction equation of vehicle responses with  $N_p$  prediction horizon and  $N_c$  control horizon is shown as follows ( $N_p \geq N_c$ ):

$$\mathbf{Y}^{up}(k) = \Psi^{up} \mathbf{z}(k) + \Theta^{up} \mathbf{V}(k) \quad (21)$$

where  $\mathbf{Y}^{up}(k)$  is the predictive control output sequence.  $\mathbf{V}(k)$  is the future control input sequence. And

$$\mathbf{Y}^{up}(k) = \begin{bmatrix} \mathbf{y}^{up}(k+1|k) \\ \mathbf{y}^{up}(k+2|k) \\ \vdots \\ \mathbf{y}^{up}(k+N_u|k) \\ \vdots \\ \mathbf{y}^{up}(k+N_p|k) \end{bmatrix}, \quad \mathbf{V}(k) = \begin{bmatrix} \mathbf{v}(k|k) \\ \mathbf{v}(k+1|k) \\ \vdots \\ \mathbf{v}(k+N_u-1|k) \end{bmatrix},$$

$$\Psi^{up} = \begin{bmatrix} \mathbf{C}^{up} \mathbf{A}_d^{up} \\ \mathbf{C}^{up} (\mathbf{A}_d^{up})^2 \\ \vdots \\ \mathbf{C}^{up} (\mathbf{A}_d^{up})^{N_u} \\ \vdots \\ \mathbf{C}^{up} (\mathbf{A}_d^{up})^{N_p} \end{bmatrix}$$

$$\Theta^{up} = \begin{bmatrix} \mathbf{C}^{up} \mathbf{B}_d^{up} & \mathbf{0} & \dots & \mathbf{0} \\ \mathbf{C}^{up} \mathbf{A}_d^{up} \mathbf{B}_d^{up} & \mathbf{C}^{up} \mathbf{B}_d^{up} & \dots & \mathbf{0} \\ \vdots & \vdots & \ddots & \vdots \\ \mathbf{C}^{up} (\mathbf{A}_d^{up})^{N_u-1} \mathbf{B}_d^{up} & \mathbf{C}^{up} (\mathbf{A}_d^{up})^{N_u-2} \mathbf{B}_d^{up} & \ddots & \mathbf{C}^{up} \mathbf{B}_d^{up} \\ \vdots & \vdots & \vdots & \vdots \\ \mathbf{C}^{up} (\mathbf{A}_d^{up})^{N_p-1} \mathbf{B}_d^{up} & \mathbf{C}^{up} (\mathbf{A}_d^{up})^{N_p-2} \mathbf{B}_d^{up} & \dots & \mathbf{C}^{up} \sum_{m=0}^{N_p-N_c} (\mathbf{A}_d^{up})^m \mathbf{B}_d^{up} \end{bmatrix}.$$

In MPC, each control channel on the control vector defined the objective as to follow its desired value as closely as possible. Therefore, a cost function quantifying the target tracking performance at each time

step is designed (Na & Cole, 2013).

$$\begin{aligned} J^{up}(k) &= \frac{1}{2} \sum_{j=1}^{N_p} \left[ (\mathbf{y}_{des}^{up}(k) - \mathbf{y}^{up}(k+j))^T \mathbf{Q}^{up} (\mathbf{y}_{des}^{up}(k) - \mathbf{y}^{up}(k+j)) \right] \\ &\quad + \frac{1}{2} \sum_{j=0}^{N_c-1} [(\mathbf{v}(k+j))^T \mathbf{R}^{up} (\mathbf{v}(k+j))] \\ &= \left\| \mathbf{Y}_{des}^{up}(k) - \mathbf{Y}^{up}(k) \right\|_{\mathbf{Q}^{up}_{MPC}}^2 + \|\mathbf{V}(k)\|_{\mathbf{R}^{up}_{MPC}}^2 \end{aligned} \quad (22)$$

where  $\mathbf{Q}^{up}_{MPC}$  is the error weight matrix, and  $\mathbf{Q}^{up}_{MPC} = \text{diag} [\mathbf{Q}^{up} \dots \mathbf{Q}^{up}]_{N_p \times N_p}$ ,

$\mathbf{Q}^{up} = \text{diag} [q_{y_1} \dots q_{y_{N_c}}]$ ,  $\mathbf{R}^{up}_{MPC}$  is the input weight matrix, and  $\mathbf{R}^{up}_{MPC} = \text{diag} [\mathbf{R}^{up} \dots \mathbf{R}^{up}]_{N_c \times N_c}$ ,  $\mathbf{R}^{up} = \text{diag} [r_{v_1} \dots r_{v_{N_p}}]$ ,  $\mathbf{Q}^{up}$  and  $\mathbf{R}^{up}$  are positive.  $\mathbf{y}_{des}^{up}$  and  $\mathbf{y}^{up}$  are the desired and actual system output sequences, and  $\mathbf{y}_{des}^{up}(k) = [\omega_{des}(k) \quad S_{Lat\_des}(k) + (S_{Lat\_des}(k) - S_{Lat\_des}(k-1)) / T_s]^T$ , according to the single-track model and the envelope boundaries (Ataei, Khajepour, & Jeon, 2018), the desired value of yaw rate  $\omega_{des}$  can be expressed by:

$$\omega_{des} = \text{sgn}(\delta_f) \times \min(\omega_{max}, \omega_S) \quad (23)$$

$$\text{where } \omega_{max} = \left| \frac{\mu g}{v_x} \right|, \quad \mu \text{ is the adhesion coefficient between tire and road,}$$

$$\omega_S = \left| \frac{v_x/L}{1+Kt_x^2} \delta_f \right|, \quad K = \frac{m}{L^2} \left( \frac{a}{c_r} - \frac{b}{c_f} \right).$$

The desired lateral displacement  $S_{Lat\_des}$  can be obtained through the path preview technology (Schnelle, Wang, Su, & Jagacinski, 2017). In this study, the abovementioned desired value is obtained by the look-up table.

Considering that the cost function (22) is constrained by the system prediction equation (21), an MPC optimization problem can be obtained, which can be solved by the following method.

Substituting Eqs. (21) into (22), and defining:

$$\Xi^{up} = \mathbf{Y}_{des}^{up} - \Psi^{up} \mathbf{z}(k) \quad (24)$$

Therefore, Eq. (22) translates into:

$$J(k) = \left\| -\Theta^{up} \mathbf{V}(k) + \Xi^{up} \right\|_{\mathbf{Q}^{up}_{MPC}}^2 + \|\mathbf{V}(k)\|_{\mathbf{R}^{up}_{MPC}}^2 \quad (25)$$

or it can be written as the least-squares form:

$$\begin{aligned} &\left\| \begin{bmatrix} S_{\mathbf{Q}^{up}_{MPC}} (-\Theta^{up} \mathbf{V}(k) + \Xi^{up}) \\ S_{\mathbf{R}^{up}_{MPC}} \mathbf{V}(k) \end{bmatrix} \right\|^2 \\ &= \left\| \begin{bmatrix} -S_{\mathbf{Q}^{up}_{MPC}} \Theta^{up} \\ S_{\mathbf{R}^{up}_{MPC}} \end{bmatrix} \mathbf{V}(k) + \begin{bmatrix} S_{\mathbf{Q}^{up}_{MPC}} \Xi^{up} \\ \mathbf{0} \end{bmatrix} \right\|^2 = 0 \end{aligned} \quad (26)$$

$$\text{where } \mathbf{Q}^{up}_{MPC} = \mathbf{S}_{\mathbf{Q}^{up}_{MPC}}^T \mathbf{S}_{\mathbf{Q}^{up}_{MPC}} \text{ and } \mathbf{R}^{up}_{MPC\_fl} = \mathbf{S}_{\mathbf{R}^{up}_{MPC\_fl}}^T \mathbf{S}_{\mathbf{R}^{up}_{MPC\_fl}}.$$

According to the description of Na and Cole (2013), the problem of this form can be solved via the QR algorithm.

$$\mathbf{V}(k) = \begin{bmatrix} -S_{\mathbf{Q}^{up}_{MPC}} \Theta^{up} \\ S_{\mathbf{R}^{up}_{MPC}} \end{bmatrix} \backslash \left( - \begin{bmatrix} S_{\mathbf{Q}^{up}_{MPC}} \Xi^{up} \\ \mathbf{0} \end{bmatrix} \right) \quad (27)$$

where the backslash operator “\” can be used to calculate the least-squares solutions in MATLAB.

According to the receding horizon idea of MPC, take the first column of the future input sequence  $\mathbf{V}(k)$  as the optimal control input  $\mathbf{v}$ . The virtual control vector  $\mathbf{v}$  is thus obtained. Then, the actual control vector  $\mathbf{u}$  can be calculated via Eq. (19), and the decoupling matrix according

to Step 2 is:

$$\begin{aligned} \mathbf{D}(\mathbf{x}^{up}) &= \begin{bmatrix} L_{\hat{g}_1} h_1 & L_{\hat{g}_2} h_1 \\ L_{\hat{g}_1} L_{\hat{f}} h_2 & L_{\hat{g}_2} L_{\hat{f}} h_2 \end{bmatrix} \\ &= \begin{bmatrix} 2ac_f \cos \delta_f & 1 \\ \frac{I_z}{2c_f \cos \delta_f} & \frac{I_z}{m} \\ \frac{2}{m} & 0 \end{bmatrix} \end{aligned} \quad (28)$$

and

$$\mathbf{b}(\mathbf{x}^{up}) = \begin{bmatrix} L_f h_1 \\ L_f^2 h_2 \end{bmatrix} = \begin{bmatrix} \hat{f}_2(\mathbf{x}^{up}) \\ \hat{f}_1(\mathbf{x}^{up}) \end{bmatrix} \quad (29)$$

#### 4. Cooperative game based lower decision allocation strategy

The lower-level control scheme is shown in the block diagram of Fig. 3. In a theoretic game, the Pareto equilibrium represents a situation where no player is willing to change their strategy unilaterally since they will not gain any more by doing so (Na & Cole, 2019). In this section, an actuators interaction paradigm is proposed based on the principle of Pareto equilibrium in the DMPC-based cooperative game approach. This generally involves three steps: (1) the four in-wheel motors are modeled as the four players in the cooperative game, and their performances are represented by the quadratic cost functions which hold the global objective; (2) four sub-optimization problems are constructed based on the four cost functions; (3) the convex iteration approach is employed to derive the analytical solutions of the game in a Pareto equilibrium sense. It can be seen from Fig. 3 that two kinds of communication channels exist in the lower-level controller, namely the channel of the targets and the channel of the player's action. The first channel enables the players to evaluate one another's desired system states, and the four players tend to hold a global desired state objective synchronously. The second channel allows each player to keep track of how its own action influences the other player's action as well as the impact of their actions on the vehicle states.

##### 4.1. Design of the predictive model

Before designing the predictive model, the system (12) should be extended to meet more performance requirements. To avoid the longitudinal tire forces saturation, each tire should have a smaller tire utilization rate  $\eta_{ij}$  which can be described as:

$$\eta_{ij} = \frac{F_{xij}^2 + F_{yij}^2}{(\mu F_{zij})^2} \leq 1 \quad (30)$$

The differential of the tire utilization rate is derived as follows:

$$\dot{\eta}_{ij} = -\frac{2}{\mu F_{zij}} \eta_{ij} + \frac{2}{R_{eff} (\mu F_{zij})^2} T_{d,ij} - \frac{2}{(\mu F_{zij})^2} \hat{F}_{ij} + \frac{2}{(\mu F_{zij})^2} F_{yij} \quad (31)$$

The lower-level system is linearized for the requirements of the cooperative game method. The vehicle system (12) is linearized based on the assumption that the vehicle steering angle is small, thus  $\sin\theta \approx 0$ ,  $\cos\theta \approx 1$ . Integrate Eq. (31) into the system (12) and discretize the system using the Euler method. The linear time-varying state-space equation is shown as follows:

$$\begin{cases} \mathbf{x}^{low}(k+1) = \mathbf{A}_d^{low}(k) \mathbf{x}^{low}(k) + \mathbf{B}_d^{low}(k) \mathbf{ET}_d(k) \\ + \Omega_d(k) \Lambda(k) \\ \mathbf{y}^{low}(k) = \mathbf{C}^{low} \mathbf{x}^{low}(k) \end{cases} \quad (32)$$

where  $\Omega_d(k) \Lambda(k)$  represents the effect of the lateral tire forces and the potential additive faults, and

$$\mathbf{x}^{low}(k) = [v_x(k) \quad \omega_x(k) \quad \eta_{fl}(k) \quad \eta_{fr}(k) \quad \eta_{rl}(k) \quad \eta_{rr}(k)]^T,$$

$$\mathbf{y}^{low}(k) = [v_x(k) \quad \omega_x(k) \quad \sum_{ij=fl,fr,rl,rr} \eta_{ij}(k)],$$

$$\begin{aligned} \mathbf{A}_d^{low}(k) &= \mathbf{I}_6 \\ &+ \left[ \begin{array}{cc|cc} 0 & v_y(k) & 0 & 0 \\ 0 & 0 & 0 & 0 \\ \hline 0 & 0 & \text{diag} \left( -\frac{2}{F_{zfl}(k)} \quad -\frac{2}{F_{zfr}(k)} \quad -\frac{2}{F_{zrl}(k)} \quad -\frac{2}{F_{zrr}(k)} \right) & \end{array} \right] T_s, \\ \mathbf{B}_d^{low}(k) &= \frac{1}{R_{eff}} \cdot [\mathbf{B}_T^{low} \quad \mathbf{B}_\eta(k)]^T \cdot T_s, \quad \mathbf{B}_T^{low} = \begin{bmatrix} \frac{1}{m} & \frac{1}{m} & \frac{1}{m} & \frac{1}{m} \\ -\frac{t_f}{I_z} & \frac{t_f}{I_z} & -\frac{t_r}{I_z} & \frac{t_r}{I_z} \end{bmatrix} \\ \mathbf{B}_\eta(k) &= \text{diag} \left[ \frac{2}{(\mu F_{zfl}(k))^2} \quad \frac{2}{(\mu F_{zfr}(k))^2} \quad \frac{2}{(\mu F_{zrl}(k))^2} \quad \frac{2}{(\mu F_{zrr}(k))^2} \right], \\ \Omega_d(k) &= \left[ \begin{array}{cc|cc} \mathbf{B}_T^{low} & 0_{2 \times 4} \\ -\mathbf{B}_\eta(k) & \mathbf{B}_\eta(k) \end{array} \right] \cdot T_s, \\ \mathbf{\Lambda}(k) &= [\hat{F}_{fl}(k) \quad \hat{F}_{fr}(k) \quad \hat{F}_{rl}(k) \quad \hat{F}_{rr}(k) \quad F_{yfl}(k) \quad F_{yfr}(k) \quad F_{yrl}(k) \quad F_{yrr}(k)]^T. \\ \mathbf{C}^{low} &= \begin{bmatrix} 1 & 0 & 0 & 0 & 0 & 0 \\ 0 & 1 & 0 & 0 & 0 & 0 \\ 0 & 0 & 1 & 1 & 1 & 1 \end{bmatrix}. \end{aligned}$$

To facilitate the application of differential game in the following, and improve the real-time performance of the control method, it is assumed that  $\mathbf{A}_d^{low}$ ,  $\mathbf{B}_d^{low}$ ,  $\mathbf{B}_\eta$ ,  $\Omega_d$  and  $\mathbf{\Lambda}$  are time-invariant.

In the framework of the DMPC-based cooperative game, a predictive system model is needed to evaluate the future system outputs. The prediction equation can be obtained by iterating Eq. (32)  $N_p$  times. Besides, it has the next  $N_c$  control horizon steps of control signals ( $N_p \geq N_c$ ). In this section,  $N_p = N_c = N$  is taken for convenience.

$$\begin{aligned} \mathbf{Y}^{low}(k) &= \Psi^{low} \mathbf{x}^{low}(k) + \Theta_{fl}^{low} \mathbf{T}_{d,fl}^{MPC}(k) + \Theta_{fr}^{low} \mathbf{T}_{d,fr}^{MPC}(k) \\ &+ \Theta_{rl}^{low} \mathbf{T}_{d,rl}^{MPC}(k) + \Theta_{rr}^{low} \mathbf{T}_{d,rr}^{MPC}(k) + \Theta_\Omega \end{aligned} \quad (33)$$

where

$$\begin{aligned} \mathbf{Y}^{low}(k) &= \begin{bmatrix} \mathbf{y}^{low}(k+1|k) \\ \mathbf{y}^{low}(k+2|k) \\ \vdots \\ \mathbf{y}^{low}(k+N|k) \end{bmatrix}, \quad \Psi^{low} = \begin{bmatrix} \mathbf{C}^{low} \mathbf{A}_d^{low} \\ \mathbf{C}^{low} (\mathbf{A}_d^{low})^2 \\ \vdots \\ \mathbf{C}^{low} (\mathbf{A}_d^{low})^N \end{bmatrix}, \\ \Theta_{ij}^{low} &= \mathbf{H} \left( \mathbf{I}_N \otimes \left( \mathbf{B}_{d,n}^{low} \mathbf{e}_{ij} \right) \right), \end{aligned}$$

$$\begin{aligned} \mathbf{H} &= \begin{bmatrix} \mathbf{C}^{low} & \mathbf{0} & \cdots & \mathbf{0} \\ \mathbf{C}^{low} \mathbf{A}_d^{low} & \mathbf{C}^{low} & \cdots & \mathbf{0} \\ \vdots & \vdots & \ddots & \vdots \\ \mathbf{C}^{low} (\mathbf{A}_d^{low})^{N-1} & \mathbf{C}^{low} (\mathbf{A}_d^{low})^{N-2} & \cdots & \mathbf{C}^{low} \end{bmatrix}, \\ \mathbf{T}_{d,ij}^{MPC}(k) &= \begin{bmatrix} T_{d,ij}(k|k) \\ T_{d,ij}(k+1|k) \\ \vdots \\ T_{d,ij}(k+N-1|k) \end{bmatrix}, \end{aligned}$$

$$\Theta_\Omega = \mathbf{H} (\mathbf{I}_N \otimes (\Omega_d \mathbf{\Lambda})).$$

where the subscript  $n$  of  $\mathbf{B}_{d,n}^{low}$  denotes the  $n$ th column of the matrix  $\mathbf{B}_d^{low}$ , and  $n := \{1, 2, 3, 4\}$  corresponding to the  $fl$ ,  $fr$ ,  $rl$  and  $rr$  in-wheel motors, respectively  $\otimes$  is the symbol of the Kronecker product.

##### 4.2. Cost function of players

The four in-wheel motors are modeled as the players in the form of the quadratic cost function. Since in a cooperative game, each player pays attention to the global objective, the cost function constructed

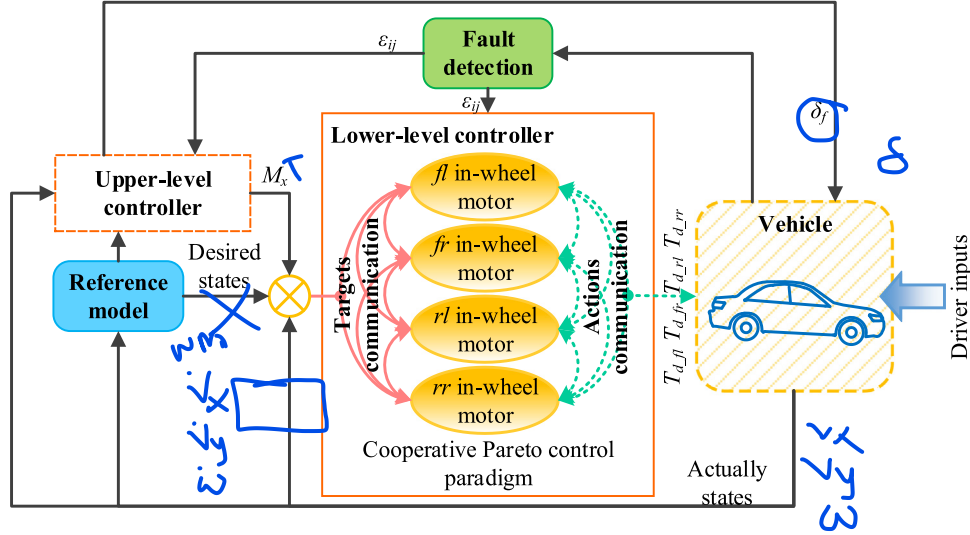


Fig. 3. Block diagram of the cooperative game based lower-level control scheme.

needs to minimize the error of global states and player's output simultaneously. Therefore, the cost functions of the in-wheel motors can be formulated by the follows:

$$\begin{aligned}
 J_n^{low}(k) &= \frac{1}{2} \sum_{j=0}^{N-1} \left[ \sum_{i=1,2,3,4} (\mathbf{y}_{des}^{low}(k) - \mathbf{y}^{low}(k+j))^T \rho_i \mathbf{Q}_i^{low} \right. \\
 &\quad \times \left. (\mathbf{y}_{des}^{low}(k) - \mathbf{y}^{low}(k+j)) \right] \\
 &+ \frac{1}{2} \sum_{j=0}^{N-1} \left[ T_{d,ij}(k+j) \left( \rho_n r_{fl}^{low} \right) T_{d,ij}(k+j) \right] + \mathbf{x}^{low}(k+N)^T \\
 &\quad \times \mathbf{P} \mathbf{x}^{low}(k+N) \\
 &= \|\mathbf{Y}_{des}^{low}(k) - \mathbf{Y}^{low}(k)\|_{\mathbf{Q}_{MPC}^{low}}^2 + \|T_{d,ij}^{MPC}(k)\|_{\mathbf{R}_{MPC,ij}^{low}}^2 \\
 &\quad + \|\mathbf{x}^{low}(k+N)\|_{\mathbf{P}}^2
 \end{aligned} \tag{34}$$

where  $\rho_n$  is used to specify the task weight of the  $n$  in-wheel motor in the overall game, and  $\sum_{i=1,2,3,4} \rho_i \mathbf{Q}_i^{low}$  represents that the target of four in-wheel motors is shared,  $\sum_{i=1,2,3,4} \rho_i = 1$ ,  $\mathbf{Q}_{MPC}^{low}$  is the error weight matrix, and  $\mathbf{Q}_{MPC}^{low} = \text{diag}(\sum [\rho_1 \mathbf{Q}_1^{low} \dots \rho_4 \mathbf{Q}_4^{low}]_{N \times N})$ ,  $\mathbf{Q}_n^{low} = \text{diag} [q_1^{v_x} \ q_2^{a_x} \ q_3^{\eta_{all}}]$  denotes the target weights of in-wheel motor,  $\mathbf{R}_{MPC,ij}^{low}$  is the weight matrix of the  $ij$  in-wheel motor input, and  $\mathbf{R}_{MPC,ij}^{low} = \text{diag} (\left[ \rho_1 r_{ij}^{low} \dots \rho_4 r_{ij}^{low} \right]_{N \times N})$ .  $\mathbf{x}^{low}(k+N)^T \mathbf{P} \mathbf{x}^{low}(k+N)$  is the terminal penalty, and  $\mathbf{x}^{low}(k+N) \in \mathbf{D}$ ,  $\mathbf{D}$  is the terminal region denotes that the predicted state has to be restricted inside it at the end of each prediction,  $\mathbf{y}_{des}^{low}$  and  $\mathbf{y}^{low}$  are the desired and actual system output sequences, and  $\mathbf{y}_{des}^{low}(k) = [v_{x,des}(k) \ \omega_{x,des}(k) \ \eta_{all,des}(k)]^T$ , in which the desired longitudinal velocity  $v_{x,des}$  can be generated from the driver's accelerator/brake pedal signals and vehicle states (Wang & Wang, 2011). The desired yaw rate determined by longitudinal tire forces is obtained by the upper-level controller,  $\omega_{x,des} = M_x/I_z$ . The desired value of  $\eta_{all,des}$  is designed as 4 according to Eq. (30).

**Remark 1.** The target communication channel in Fig. 3 is achieved via the cost functions (34), and the global state vector of the system is shared with each player.

**Remark 2.** In the cost functions (34), there are two kinds of weight coefficients that have a significant influence on the game results, namely the target weight  $q_i^x$  and the task weight  $\rho_n$ . The former represents the player's preference for targets, and the latter represents the proportion of tasks assigned to players.

Based on the DMPC theory, construct the following optimization problem for each player

$$\begin{aligned}
 \min \quad J_n^{low}(k) &= \|\mathbf{Y}_{des}^{low}(k) - \mathbf{Y}^{low}(k)\|_{\mathbf{Q}_{MPC}^{low}}^2 + \|T_{d,ij}^{MPC}(k)\|_{\mathbf{R}_{MPC,ij}^{low}}^2 \\
 \text{s.t.} \quad \mathbf{Y}^{low}(k) &= \Psi^{low} \mathbf{x}^{low}(k) + \sum_{ij=f,l,r,r} \Theta_{ij}^{low} T_{d,ij}^{MPC}(k) + \Theta_{\Omega} \\
 \mathbf{x}^{low}(k+N) &\in \mathbf{D}
 \end{aligned} \tag{35}$$

#### 4.3. Closed-loop stability analysis

The closed-loop stability of the system will be described in this subsection based on the terminal equality constraint (Liu, Yu, Gao, & Chen, 2015). In this method, the terminal state of the control horizon is forced to return to the equilibrium point through the terminal equation constraint. Therefore,  $\mathbf{x}^{low}(k+N) = \mathbf{0}$  and  $\mathbf{D} = \{\mathbf{0}\}$ .

**Theorem 1.** Assume that there exist linear feedbacks  $T_{d,ij}^*(k) = \mathbf{K}_{ij} \mathbf{x}^{low}(k)$  such that the following conditions hold:

- (1) The system (32) is observable.
- (2)  $\Omega_d(k) \Lambda(k) \approx \mathbf{0}$ .

Then

- (a) The proposed algorithm is feasible for all time step  $k \geq 0$ .
- (b) The system (32) in closed-loop is asymptotically stable.

Because the value of  $\Omega_d(k) \Lambda(k)$  shown in Eq. (32) is small enough, the condition (2) of Theorem 1 can be satisfied.

**Proof.** According to Maestre et al. (2011), prove that under given assumptions,

$$\begin{aligned}
 J^{low}(k) &= \sum_n J_n^{low}(k) \\
 &= \frac{1}{2} \sum_{j=0}^{N-1} \left[ \|\Delta \mathbf{y}^{low}(k+j|k)\|_{\mathbf{Q}}^2 + \|T_d(k+j|k)\|_{\mathbf{R}}^2 \right] \\
 &\quad + 4 \|\mathbf{x}^{low}(k+N)\|_{\mathbf{P}}^2
 \end{aligned} \tag{36}$$

is a decreasing sequence of values with a lower bound, and  $J(k)$  is also a Lyapunov function of the closed-loop system. where  $\mathbf{Q} = 4 \sum \rho_i \mathbf{Q}_i^{low}$ ,  $\mathbf{R} = \text{diag} [\rho_1 r_{fl}^{low} \ \rho_2 r_{fr}^{low} \ \rho_3 r_{rl}^{low} \ \rho_4 r_{rr}^{low}]$ ,  $\Delta \mathbf{y}^{low}(k+j|k) = \mathbf{y}_{des}^{low}(k|k) - \mathbf{y}^{low}(k+j|k)$ .

Assume that the optimization problem (35) has a solution at time step  $k$  as:

$$\mathbf{T}^*(k) = \begin{bmatrix} \mathbf{T}_d^*(k|k) \\ \mathbf{T}_d^*(k+1|k) \\ \vdots \\ \mathbf{T}_d^*(k+N-1|k) \end{bmatrix} \quad (37)$$

The corresponding prediction status and prediction output are as follows:

$$\{\mathbf{x}^{low\_*}(k+1|k) \quad \mathbf{x}^{low\_*}(k+2|k) \quad \dots \quad \mathbf{x}^{low\_*}(k+N-1|k) \quad \mathbf{0}\} \quad (38)$$

$$\{\Delta\mathbf{y}^{low\_*}(k+1|k) \quad \Delta\mathbf{y}^{low\_*}(k+2|k) \quad \dots \quad \Delta\mathbf{y}^{low\_*}(k+N-1|k) \quad \mathbf{0}\} \quad (39)$$

The value of Eq. (36) is:

$$J^*(k) = \sum_{j=0}^{N-1} \left[ \|\Delta\mathbf{y}^{low\_*}(k+j|k)\|_Q^2 + \|\mathbf{T}_d^*(k+j|k)\|_R^2 \right] \quad (40)$$

The closed-loop control law defined by Theorem 1 is:

$$\mathbf{T}_d(k) \stackrel{def}{=} \mathbf{T}_d^*(k|k) \quad (41)$$

$$\text{where } \mathbf{T}_d^*(k|k) = \begin{bmatrix} \mathbf{T}_{d\_fl}^*(k|k) & \mathbf{T}_{d\_fr}^*(k|k) & \mathbf{T}_{d\_rl}^*(k|k) & \mathbf{T}_{d\_rr}^*(k|k) \end{bmatrix}^T.$$

At time step  $k+1$ , assume a preselected control sequence:

$$\mathbf{T}^*(k+1) = \begin{bmatrix} \mathbf{T}_d(k+1|k+1) \\ \mathbf{T}_d(k+2|k+1) \\ \vdots \\ \mathbf{T}_d(k+N-1|k+1) \\ \mathbf{T}_d(k+N|k+1) \end{bmatrix} \stackrel{def}{=} \begin{bmatrix} \mathbf{T}_d^*(k+1|k) \\ \mathbf{T}_d^*(k+2|k) \\ \vdots \\ \mathbf{T}_d^*(k+N-1|k) \\ \mathbf{0} \end{bmatrix} \quad (42)$$

The last element of the preselected control sequence is zero, because  $\mathbf{x}^{low}(k+N) = \mathbf{0}$ , if  $\mathbf{T}_d(k+N) = \mathbf{0}$  and the condition (2) of Theorem 1 is considered, then

$$\begin{aligned} \mathbf{x}^{low}(k+N+1) &= \mathbf{A}_d^{low}(k+N)\mathbf{x}^{low}(k+N) + \mathbf{B}_d^{low}(k+N)\mathbf{E}\mathbf{T}_d(k+N) \\ &\quad + \Omega_d(k+N)\Lambda(k+N) \\ &= \mathbf{0} \end{aligned} \quad (43)$$

This keeps the system at the equilibrium point. The state sequence and output sequence corresponding to (42) are as follows:

$$\mathbf{x}^{low}(k+1+i|k+1) = \begin{cases} \mathbf{x}^{low\_*}(k+1+i|k), & i = 0, \dots, N-1 \\ \mathbf{0}, & i = N \end{cases} \quad (44)$$

$$\mathbf{y}^{low}(k+1+i|k+1) = \begin{cases} \mathbf{y}^{low\_*}(k+1+i|k), & i = 0, \dots, N-1 \\ \mathbf{0}, & i = N \end{cases} \quad (45)$$

According to Eqs. (42), (44) and (45), the value of Eq. (36) at time step  $k+1$  is:

$$\begin{aligned} J(k+1) &= \sum_{j=0}^{N-1} \left[ \|\Delta\mathbf{y}^{low}(k+1+j|k+1)\|_Q^2 + \|\mathbf{T}_d(k+1+j|k+1)\|_R^2 \right] \\ &= \sum_{j=0}^{N-2} \left[ \|\Delta\mathbf{y}^{low\_*}(k+1+j|k)\|_Q^2 + \|\mathbf{T}_d^*(k+1+j|k)\|_R^2 \right] \\ &= \sum_{j=1}^{N-1} \left[ \|\Delta\mathbf{y}^{low\_*}(k+j|k)\|_Q^2 + \|\mathbf{T}_d^*(k+j|k)\|_R^2 \right] \\ &= \sum_{j=0}^{N-1} \left[ \|\Delta\mathbf{y}^{low\_*}(k+j|k)\|_Q^2 + \|\mathbf{T}_d^*(k+j|k)\|_R^2 \right] \\ &\quad - \|\Delta\mathbf{y}^{low\_*}(k|k)\|_Q^2 - \|\mathbf{T}_d^*(k|k)\|_R^2 \\ &= J^*(k) - \|\Delta\mathbf{y}^{low\_*}(k|k)\|_Q^2 - \|\mathbf{T}_d^*(k|k)\|_R^2 \\ &\leq J^*(k) \end{aligned} \quad (46)$$

Therefore,  $J(k+1)$  is bounded, and the preselected control sequence (42) is a feasible solution to the optimization problem (35) at time step  $k+1$ . Theorem 1 (a) is proved.

If there is an optimal solution to the optimization problem at time step  $k+1$ , the value of the optimized solution  $J^*(k+1)$  will not be

greater than that of the feasible solution.

$$J^*(k+1) \leq J(k+1) \leq J^*(k) \quad (47)$$

It can be seen that the cost function sequence  $J(k)$  is monotonically non-increasing, and its lower bound is zero. The closed-loop system is asymptotic stable. Theorem 1 (b) is proved.  $\square$

#### 4.4. Solution of cooperative game

In the cooperative game, each player keeps track of how its input affects the output of other players as well as their output. This is in general achieved by simultaneously solving the four predictive control problems (35). Continuing to follow Na (Na & Cole, 2015) and Rawlings (Rawlings & Mayne, 2016), the solution of the cooperative game will be derived in this section.

The error between the actual value and desired value of the  $ij$  in-wheel motor is defined as:

$$\Xi_{ij}^{low}(k) = \mathbf{Y}_{des}^{low}(k) - \Psi^{low}\mathbf{x}^{low}(k) - \sum_{pq \in S \setminus \{ij\}} \Theta_{pq}^{low} \mathbf{T}_{d\_pq}^{MPC}(k) - \Theta_\Omega \quad (48)$$

where set  $S = \{fl, fr, rl, rr\}$ ,  $S \setminus \{ij\}$  denotes the  $S$  set without  $ij$ .

Then, substituting Eq. (48) and  $\mathbf{x}^{low}(k+N) = \mathbf{0}$  into the player's cost function, the optimization problem (35) can be rewritten as:

$$\min J_n^{low}(k) = \left\| -\Theta_{ij}^{low} \mathbf{T}_{d\_ij}^{MPC}(k) + \Xi_{ij}^{low}(k) \right\|_{Q_{MPC}^{low}}^2 + \left\| \mathbf{T}_{d\_ij}^{MPC}(k) \right\|_{R_{MPC,ij}^{low}}^2 \quad (49)$$

or it can be written as the least-squares form

$$\begin{aligned} J_n^{low}(k) &= \left\| -S_{Q_{MPC}^{low}} \begin{pmatrix} \Theta_{ij}^{low} \mathbf{T}_{d\_ij}^{MPC}(k) - \Xi_{ij}^{low}(k) \\ S_{R_{MPC,ij}^{low}} \mathbf{T}_{d\_ij}^{MPC}(k) \end{pmatrix} \right\|^2 \\ &= \left\| \begin{pmatrix} -S_{Q_{MPC}^{low}} \Theta_{ij}^{low} \\ S_{R_{MPC,ij}^{low}} \end{pmatrix} \mathbf{T}_{d\_ij}^{MPC}(k) + \begin{pmatrix} S_{Q_{MPC}^{low}} \\ 0 \end{pmatrix} \Xi_{ij}^{low}(k) \right\|^2 \end{aligned} \quad (50)$$

where  $Q_{MPC}^{low} = S_{Q_{MPC}^{low}}^T S_{Q_{MPC}^{low}}$  and  $R_{MPC,ij}^{low} = S_{R_{MPC,ij}^{low}}^T S_{R_{MPC,ij}^{low}}$ .

The optimal solution of (50) is shown as:

$$\mathbf{T}_{d\_ij}^*(k) = \underbrace{\left[ \begin{bmatrix} -S_{Q_{MPC}^{low}} \Theta_{ij}^{low} \\ S_{R_{MPC,ij}^{low}} \end{bmatrix} \backslash \left( -\begin{bmatrix} S_{Q_{MPC}^{low}} \\ 0 \end{bmatrix} \Xi_{ij}^{low}(k) \right) \right]}_{L_n} \Xi_{ij}^{low}(k) \quad (51)$$

where the superscript \* denotes the optimal solution.

Substitution of Eq. (48) into (51), then the following equation holds:

$$\mathbf{T}_{d\_ij}^*(k) = \underbrace{[-\mathbf{L}_n \Psi^{low} \quad \mathbf{L}_n]}_{\Gamma_n} \underbrace{\begin{bmatrix} \mathbf{x}^{low}(k) \\ \mathbf{Y}_{des}^{low}(k) \end{bmatrix}}_{Z_D} - \sum_{pq \in S \setminus \{ij\}} \mathbf{L}_n \Theta_{pq}^{low} \mathbf{T}_{d\_pq}^{MPC}(k) - \mathbf{L}_n \Theta_\Omega \quad (52)$$

Eq. (52) can be rewritten as the matrix form:

$$\begin{aligned} \begin{bmatrix} \mathbf{T}_{d\_fl}^*(k) \\ \mathbf{T}_{d\_fr}^*(k) \\ \mathbf{T}_{d\_rl}^*(k) \\ \mathbf{T}_{d\_rr}^*(k) \end{bmatrix} &= \begin{bmatrix} \Gamma_1 & \mathbf{0} & \mathbf{0} & \mathbf{0} \\ \mathbf{0} & \Gamma_2 & \mathbf{0} & \mathbf{0} \\ \mathbf{0} & \mathbf{0} & \Gamma_3 & \mathbf{0} \\ \mathbf{0} & \mathbf{0} & \mathbf{0} & \Gamma_4 \end{bmatrix} \begin{bmatrix} Z_D \\ Z_D \\ Z_D \\ Z_D \end{bmatrix} \\ &\quad - \begin{bmatrix} \mathbf{0} & L_1 \Theta_{fr}^{low} & L_1 \Theta_{rl}^{low} & L_1 \Theta_{rr}^{low} \\ L_2 \Theta_{fl}^{low} & \mathbf{0} & L_2 \Theta_{rl}^{low} & L_2 \Theta_{rr}^{low} \\ L_3 \Theta_{fl}^{low} & L_3 \Theta_{fr}^{low} & \mathbf{0} & L_3 \Theta_{rr}^{low} \\ L_4 \Theta_{fl}^{low} & L_4 \Theta_{fr}^{low} & L_4 \Theta_{rl}^{low} & \mathbf{0} \end{bmatrix} \\ &\quad \times \begin{bmatrix} \mathbf{T}_{d\_fl}(k) \\ \mathbf{T}_{d\_fr}(k) \\ \mathbf{T}_{d\_rl}(k) \\ \mathbf{T}_{d\_rr}(k) \end{bmatrix} - \begin{bmatrix} \mathbf{L}_1 \\ \mathbf{L}_2 \\ \mathbf{L}_3 \\ \mathbf{L}_4 \end{bmatrix} \Theta_\Omega \end{aligned} \quad (53)$$

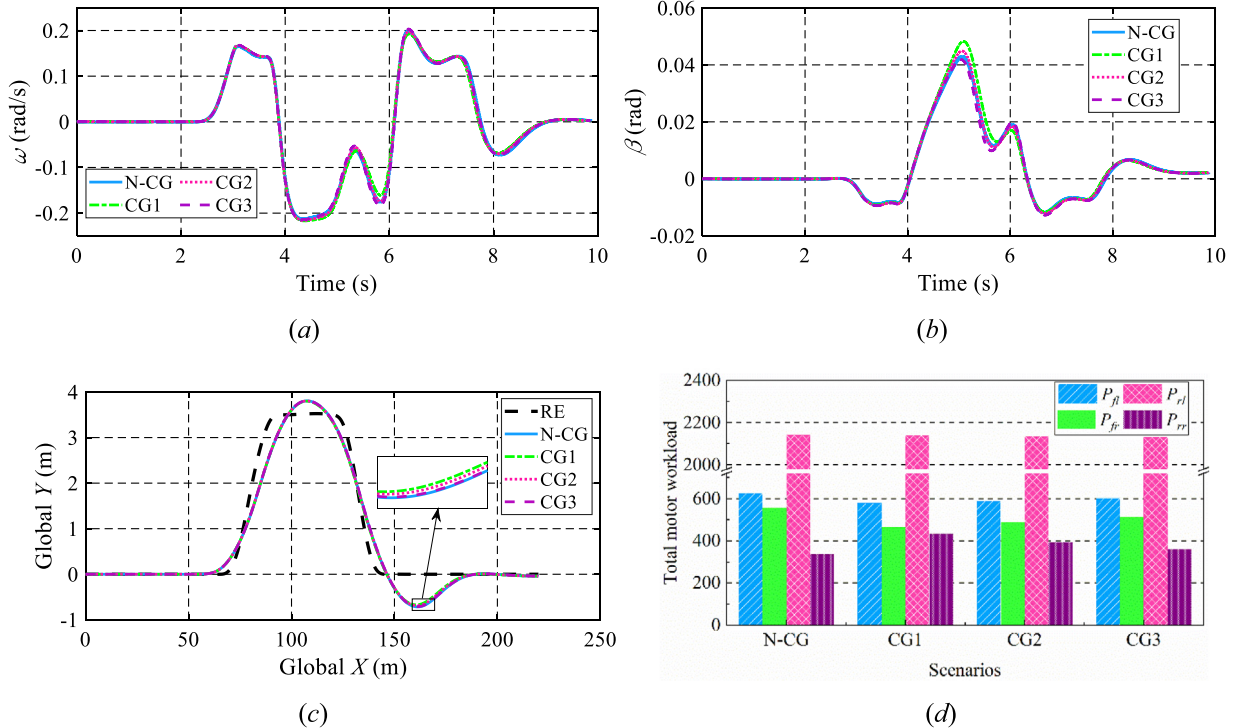


Fig. 4. Control results of different control parameters. (a) Yaw rate. (b) Side-slip angle. (c) Trajectory. (d) Total motor workload.

**Remark 3.** It can be seen from Eq. (53) that the optimal output sequence of each in-wheel motor  $T_{d_{ij}}^*(k)$  depends not only on the system state  $x^{low}(k)$  and its desired sequence  $Y_{des}^{low}(k)$ , but also on the control output sequence of the other in-wheel motors  $T_{d_{ij}}(k)$ . This phenomenon indicates that Eq. (53) has the foundation of the two kinds of communication channels shown in Fig. 3. However, since the strategies of other players are unknown, communication is not carried out.

The communication among players and the derivation of analytical solutions can be achieved through a convex iteration approach whose detail can be found in the relevant literature (Rawlings & Mayne, 2016). This method introduces an iteration auxiliary equation:

$$\begin{bmatrix} T_{d_{fl}}(k)^{[p+1]} \\ T_{d_{fr}}(k)^{[p+1]} \\ T_{d_{rl}}(k)^{[p+1]} \\ T_{d_{rr}}(k)^{[p+1]} \end{bmatrix} = \begin{bmatrix} w_1 I & 0 & 0 & 0 \\ 0 & w_2 I & 0 & 0 \\ 0 & 0 & w_3 I & 0 \\ 0 & 0 & 0 & w_4 I \end{bmatrix} \begin{bmatrix} T_{d_{fl}}^*(k)^{[p]} \\ T_{d_{fr}}^*(k)^{[p]} \\ T_{d_{rl}}^*(k)^{[p]} \\ T_{d_{rr}}^*(k)^{[p]} \end{bmatrix} + \begin{bmatrix} (1-w_1) I & 0 & 0 & 0 \\ 0 & (1-w_2) I & 0 & 0 \\ 0 & 0 & (1-w_3) I & 0 \\ 0 & 0 & 0 & (1-w_4) I \end{bmatrix} \times \begin{bmatrix} T_{d_{fl}}(k)^{[p]} \\ T_{d_{fr}}(k)^{[p]} \\ T_{d_{rl}}(k)^{[p]} \\ T_{d_{rr}}(k)^{[p]} \end{bmatrix} \quad (54)$$

where  $p \in \mathbb{Z}^+$  denote the integer-valued iteration steps in the optimization problem.  $w_1, w_2, w_3$ , and  $w_4$  are iteration weights which satisfy  $0 < w_i < 1$  and  $w_1 + w_2 + w_3 + w_4 = 1$ .

Finally arrived at  $p + 1 = p \rightarrow \infty$  as  $p$  increases. Eqs. (53) and (54) are transformed into:

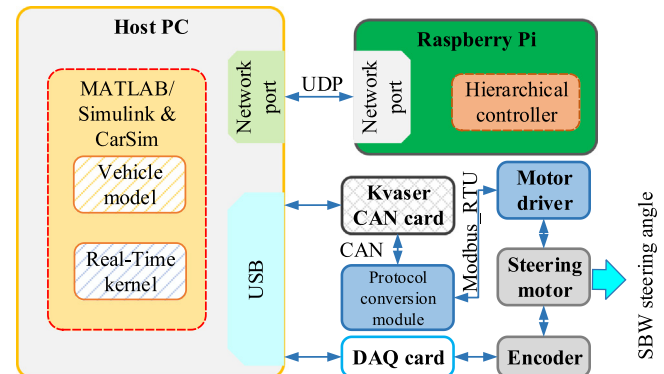


Fig. 5. The schematic diagram of the HIL platform.

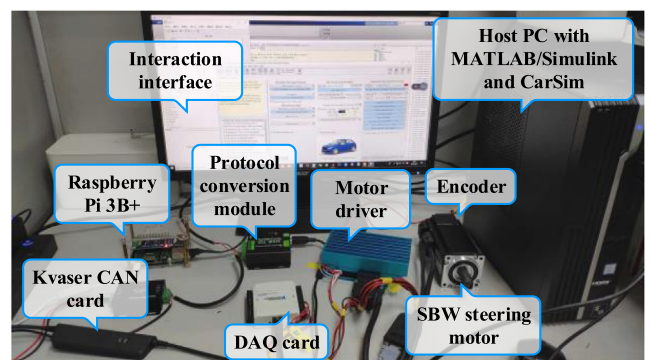


Fig. 6. Basic facilities of the HIL platform.

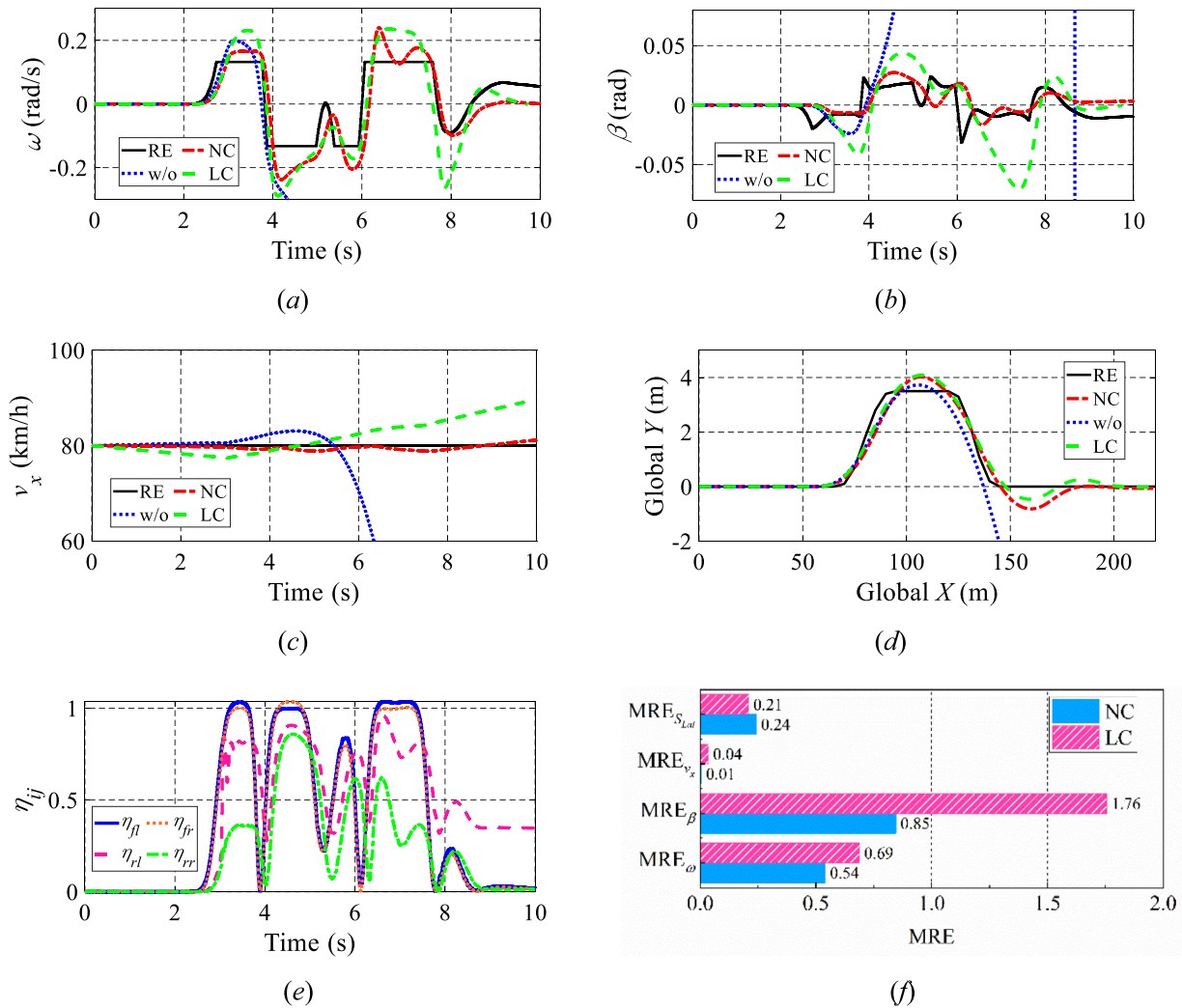


Fig. 7. Control results in the stuck-at-fixed-level fault case. (a) Yaw rate. (b) Side-slip angle. (c) Longitudinal velocity. (d) Trajectory. (e) Tire utilization rate. (f) MRE.

**Table 1**  
Vehicle parameters used for the simulation.

Parameters	Values	Parameters	Values
$m$	1480 kg	$t_r$	1.54 m
$I_z$	1536.70 kg m <sup>2</sup>	$R_w$	0.32 m
$L$	2.58 m	$c_f$	54 458 N/rad
$a$	1.22 m	$c_r$	74 490 N/rad
$b$	1.36 m	$T_{max}$	400 N m
$t_f$	1.64 m		

$$\begin{bmatrix} \mathbf{T}_{d\_fl}^*(k)^{[\infty]} \\ \mathbf{T}_{d\_fr}^*(k)^{[\infty]} \\ \mathbf{T}_{d\_rl}^*(k)^{[\infty]} \\ \mathbf{T}_{d\_rr}^*(k)^{[\infty]} \end{bmatrix} = \begin{bmatrix} \Gamma_1 & \mathbf{0} & \mathbf{0} & \mathbf{0} \\ \mathbf{0} & \Gamma_2 & \mathbf{0} & \mathbf{0} \\ \mathbf{0} & \mathbf{0} & \Gamma_3 & \mathbf{0} \\ \mathbf{0} & \mathbf{0} & \mathbf{0} & \Gamma_4 \end{bmatrix} \begin{bmatrix} \mathbf{Z}_D \\ \mathbf{Z}_D \\ \mathbf{Z}_D \\ \mathbf{Z}_D \end{bmatrix} - \begin{bmatrix} \mathbf{0} & L_1\Theta_{fr}^{low} & L_1\Theta_{rl}^{low} & L_1\Theta_{rr}^{low} \\ L_2\Theta_{fl}^{low} & \mathbf{0} & L_2\Theta_{rl}^{low} & L_2\Theta_{rr}^{low} \\ L_3\Theta_{fl}^{low} & L_3\Theta_{fr}^{low} & \mathbf{0} & L_3\Theta_{rr}^{low} \\ L_4\Theta_{fl}^{low} & L_4\Theta_{fr}^{low} & L_4\Theta_{rl}^{low} & \mathbf{0} \end{bmatrix}$$

$$\times \begin{bmatrix} \mathbf{T}_{d\_fl}(k)^{[\infty]} \\ \mathbf{T}_{d\_fr}(k)^{[\infty]} \\ \mathbf{T}_{d\_rl}(k)^{[\infty]} \\ \mathbf{T}_{d\_rr}(k)^{[\infty]} \end{bmatrix} - \begin{bmatrix} \mathbf{L}_1 \\ \mathbf{L}_2 \\ \mathbf{L}_3 \\ \mathbf{L}_4 \end{bmatrix} \Theta_{\Omega} \quad (55)$$

$$\begin{bmatrix} \mathbf{T}_{d\_fl}(k)^{[\infty]} \\ \mathbf{T}_{d\_fr}(k)^{[\infty]} \\ \mathbf{T}_{d\_rl}(k)^{[\infty]} \\ \mathbf{T}_{d\_rr}(k)^{[\infty]} \end{bmatrix} = \begin{bmatrix} w_1 \mathbf{I} & \mathbf{0} & \mathbf{0} & \mathbf{0} \\ \mathbf{0} & w_2 \mathbf{I} & \mathbf{0} & \mathbf{0} \\ \mathbf{0} & \mathbf{0} & w_3 \mathbf{I} & \mathbf{0} \\ \mathbf{0} & \mathbf{0} & \mathbf{0} & w_4 \mathbf{I} \end{bmatrix} \begin{bmatrix} \mathbf{T}_{d\_fl}^*(k)^{[\infty]} \\ \mathbf{T}_{d\_fr}^*(k)^{[\infty]} \\ \mathbf{T}_{d\_rl}^*(k)^{[\infty]} \\ \mathbf{T}_{d\_rr}^*(k)^{[\infty]} \end{bmatrix} + \begin{bmatrix} (1-w_1) \mathbf{I} & \mathbf{0} & \mathbf{0} & \mathbf{0} \\ \mathbf{0} & (1-w_2) \mathbf{I} & \mathbf{0} & \mathbf{0} \\ \mathbf{0} & \mathbf{0} & (1-w_3) \mathbf{I} & \mathbf{0} \\ \mathbf{0} & \mathbf{0} & \mathbf{0} & (1-w_4) \mathbf{I} \end{bmatrix} \quad (56)$$

$$\times \begin{bmatrix} \mathbf{T}_{d\_fl}(k)^{[\infty]} \\ \mathbf{T}_{d\_fr}(k)^{[\infty]} \\ \mathbf{T}_{d\_rl}(k)^{[\infty]} \\ \mathbf{T}_{d\_rr}(k)^{[\infty]} \end{bmatrix}$$

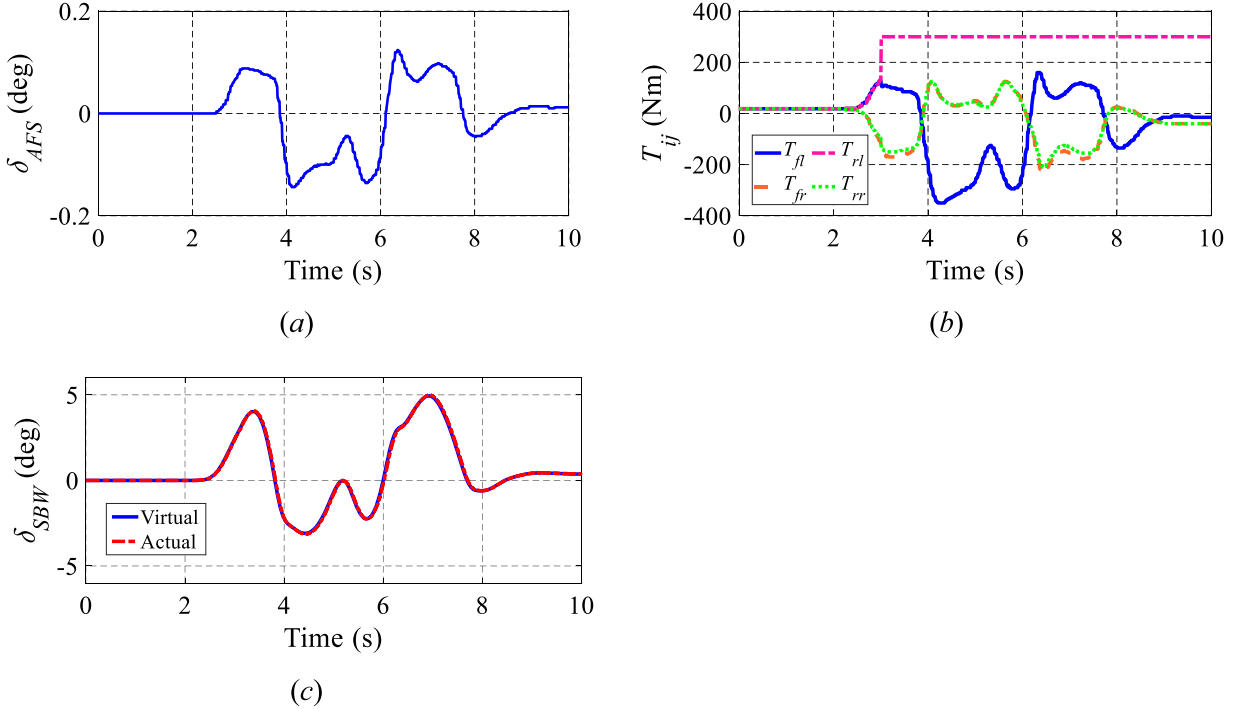


Fig. 8. NC controller outputs in the stuck-at-fixed-level fault case. (a) AFS steering angle. (b) In-wheel motor torques. (c) SBW steering angle.

Substitution of Eq. (55) into (56) yields:

$$\begin{bmatrix} \mathbf{T}_{d\_fl}(k)^{[\infty]} \\ \mathbf{T}_{d\_fr}(k)^{[\infty]} \\ \mathbf{T}_{d\_rl}(k)^{[\infty]} \\ \mathbf{T}_{d\_rr}(k)^{[\infty]} \end{bmatrix} = \begin{bmatrix} I & L_1\Theta_{fr}^{low} & L_1\Theta_{rl}^{low} & L_1\Theta_{rr}^{low} \\ L_2\Theta_{fl}^{low} & I & L_2\Theta_{rl}^{low} & L_2\Theta_{rr}^{low} \\ L_3\Theta_{fl}^{low} & L_3\Theta_{fr}^{low} & I & L_3\Theta_{rr}^{low} \\ L_4\Theta_{fl}^{low} & L_4\Theta_{fr}^{low} & L_4\Theta_{rl}^{low} & I \end{bmatrix}^{-1} \cdot \begin{bmatrix} \Gamma_1 & 0 & 0 & 0 \\ 0 & \Gamma_2 & 0 & 0 \\ 0 & 0 & \Gamma_3 & 0 \\ 0 & 0 & 0 & \Gamma_4 \end{bmatrix} \begin{bmatrix} Z_D \\ Z_D \\ Z_D \\ Z_D \end{bmatrix} - \begin{bmatrix} L_1 \\ L_2 \\ L_3 \\ L_4 \end{bmatrix} \Theta_{\Omega} \quad (57)$$

Note that the weights \$w\_1\$, \$w\_2\$, \$w\_3\$ and \$w\_4\$ disappear in the input sequence because the result is convergent (Rawlings & Mayne, 2016).

According to the receding horizon idea, take the first column of the future input sequence \$\mathbf{T}\_{d\\_ij}(k)^{[\infty]}\$ as the Pareto strategy adopted by the \$ij\$ in-wheel motor.

## 5. Simulation and RT-HIL experiment results and analysis

In this section, a comparative study is carried out to explain the inherent difference between the cooperative game and noncooperative game in coordination. Then, the effectiveness and real-time performance of the proposed FTC algorithm are tested in an RT-HIL test bench.

The full vehicle model is constructed in the CarSim combination of MATLAB/Simulink. The vehicle parameters in the tests are listed in Table 1. A built-in driver model of CarSim is chosen, and the preview time is set as 0.8 s due to the higher velocity (Wang, Zhang, Wang, Schnelle, & Wang, 2017).

### 5.1. Numerical simulation and results analysis

First, analyze the difference between the cooperative game and noncooperative game from the cost function level. The following is a recap of the derivation key points of the noncooperative game.

In a noncooperative game, the in-wheel motor focuses on pursuing its individual interest that is to minimize its individual system state objectives (Na & Cole, 2019). Hence, the cost function of players can be expressed as

$$\begin{aligned} J_n^{low}(k) &= \frac{1}{2} \sum_{j=0}^{N-1} \left[ (\mathbf{y}_{des}^{low}(k) - \mathbf{y}^{low}(k+j))^T \mathbf{Q}_n^{low} \right. \\ &\quad \times \left. (\mathbf{y}_{des}^{low}(k) - \mathbf{y}^{low}(k+j)) \right] \\ &\quad + \frac{1}{2} \sum_{j=0}^{N-1} \left[ (T_{d\_ij}(k+j))^2 (r_{fl}^{low}) \right] + \mathbf{x}^{low}(k+N)^T \\ &\quad \times \mathbf{P} \mathbf{x}^{low}(k+N) \\ &= \left\| \mathbf{Y}_{des}^{low}(k) - \mathbf{Y}^{low}(k) \right\|_{\mathbf{Q}_{n\_MPC}^{low}}^2 + \left\| \mathbf{T}_{d\_ij}^{MPC}(k) \right\|_{\mathbf{R}_{MPC\_ij}^{low}}^2 \\ &\quad + \left\| \mathbf{x}^{low}(k+N) \right\|_{\mathbf{P}}^2 \end{aligned} \quad (58)$$

where \$\mathbf{Q}\_{n\\_MPC}^{low}\$ is the error weight matrix, and \$\mathbf{Q}\_{n\\_MPC}^{low} = \text{diag}([\mathbf{Q}\_n^{low} \dots \mathbf{Q}\_n^{low}]\_{N \times N})\$.

The solutions derived from the noncooperative game are called the Nash strategies, and its derivation process is similar to the cooperative game.

By comparing the player's noncooperative cost function (58) and the cooperative cost function (34), it can be found that in the noncooperative game, the player does not take into account the other player's interest, that is, the noncooperative game only has action communication channel compared to the cooperative game. This is the key difference between the noncooperative game and the cooperative game.

The difference between the cooperative game (CG) and noncooperative game (N-CG) is further analyzed by the following numerical simulation cases. Specifically, the comparison is made under four sets of control parameters shown in Table 2. The parameters in Table 2 represents the assumption that player 4 has a different target weight than the other three players. N-CG and CG1 can be used to compare the difference between the cooperative game and noncooperative game when players hold different targets. Cases CG1-CG3 are used to illustrate the influence of player 4's increased task weights on the cooperative game. The equation shown in the following is defined to

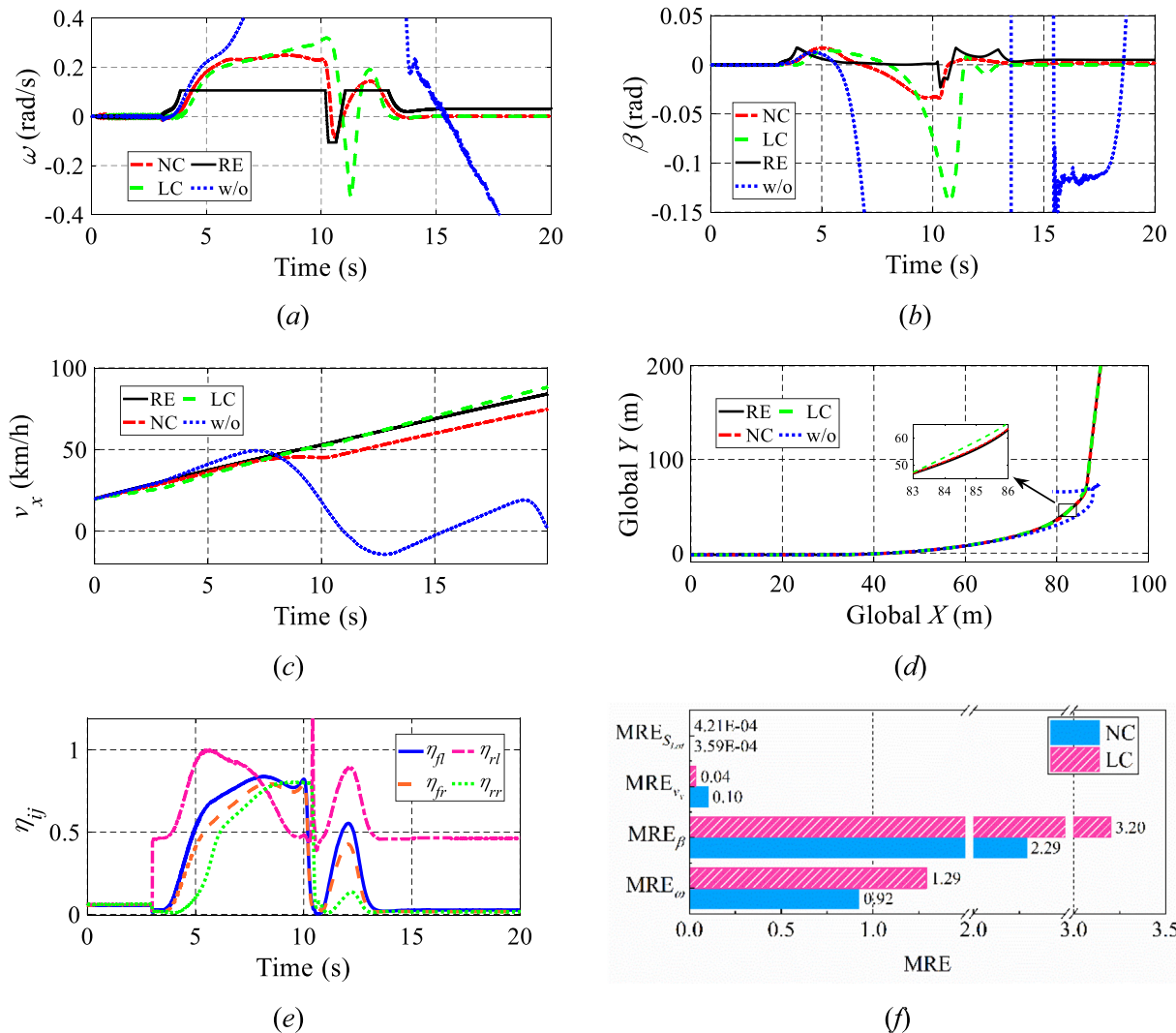


Fig. 9. Control results in the additive fault case. (a) Yaw rate. (b) Side-slip angle. (c) Longitudinal velocity. (d) Trajectory. (e) Tire utilization rate. (f) MRE.

**Table 2**  
Control parameters for comparison.

	Target weights	Task weights
N-CG	player 1-3: \$q_{n,1}^{v_x} = 0.64\$, \$q_{n,2}^{\omega_x} = 0.0121\$, \$q_{n,3}^{\eta_{all}} = 1\$	/
CG1		\$\rho_1 = \rho_2 = \rho_3 = \rho_4 = 0.25\$
CG2	player 4: \$q_{4,1}^{v_x} = 0.64\$, \$q_{4,2}^{\omega_x} = 0.0064\$, \$q_{4,3}^{\eta_{all}} = 1\$	\$\rho_1 = \rho_2 = \rho_3 = 0.24\$, \$\rho_4 = 0.28\$
CG3		\$\rho_1 = \rho_2 = \rho_3 = 0.23\$, \$\rho_4 = 0.31\$

represent the total workload of the in-wheel motors.

$$P_{ij} = \int_0^{T_i} |f_{ji}| dt \quad (59)$$

where \$T\_i\$ denotes the total maneuvering time.

The vehicle is manipulated with a double line change (DLC), in which the initial velocity \$v\_x = 80\$ km/h, the road adhesion coefficient is set as 0.45. At the time of 3 s, a stuck-at-fixed-level fault occurs in the **rl** in-wheel motor, which makes its torque stuck at 300 N m.

Fig. 4(a)–(c) illustrate the vehicle yaw rate, side-slip angle, and trajectory under different control parameters. It can be seen that the cooperative game and noncooperative game have similar control effects. This is because in the cooperative game or noncooperative game, although the target weights of the players are different, they all have the same global targets. Fig. 4(d) shows the total workload of each player in the cooperative game and noncooperative game. It can be

seen by comparing N-CG and CG1 in Fig. 4(d) that in the case where the players adopt the **Nash** strategies, the workload of the **rr** in-wheel motor is decreased with the reduction of its target weight \$q\_{4,2}^{\omega\_x}\$, and the workload of the remaining two healthy motors is increased accordingly. This means that the controllable margin of the two in-wheel motors is reduced, which hinders the controllability of the vehicle in dangerous situations. However, the workload of players can be more reasonably distributed through the state communication channel in the cooperative game. Such difference suggests that the cooperative game can weaken the impact of the individual player's target weights on global actions.

As can be seen from the comparison of CG1–CG3 in Fig. 4(d), the workload of **rr** in-wheel motor is decreased as its task weight increases and the workloads of other players are increased accordingly, that is, the target of **rr** motor has gained more respect. In summary, the player can obtain more reasonable results by evaluating the target of other players in the cooperative game framework, and the preference of game results can be changed by adjusting the task weights.

## 5.2. RT-HIL experiment validation

The schematic diagram of the HIL platform is shown in Fig. 5. It composes of a Host PC, a steering motor, a motor driver, a Raspberry Pi (3 Model B+), a Kvaser CAN card (Leaf Light v2), a NI data acquisition (DAQ) card (USB-6009), an incremental encoder, and a protocol conversion module. This test bench considers the truncation

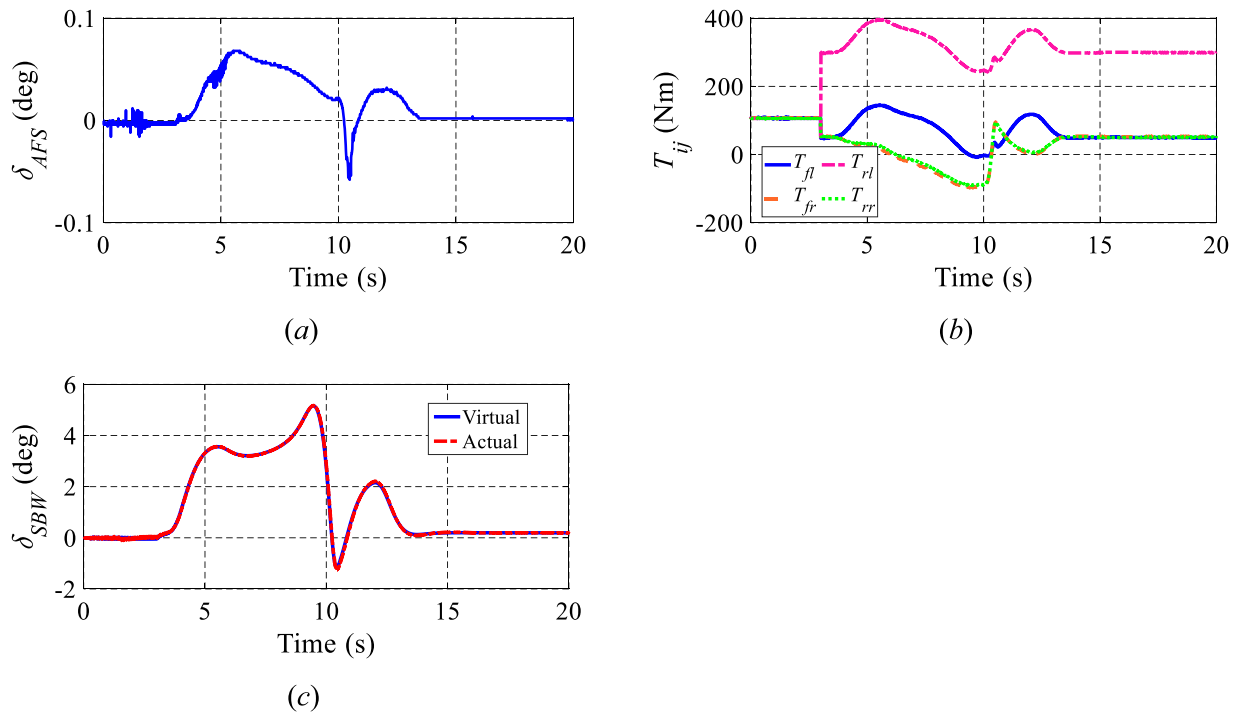


Fig. 10. NC controller outputs in the additive fault case. (a) AFS steering angle. (b) In-wheel motor torques. (c) SBW steering angle.

**Table 3**  
Control parameters used in RT-HIL.

Target weights	Task weights
Player 1-4: \$q_{n_1}^{v_x} = 0.64\$, \$q_{n_2}^{\omega_x} = 0.0121\$, \$q_{n_3}^{\eta_{all}} = 1\$	\$\rho_1 = \rho_2 = \rho_3 = \rho_4 = 0.25\$

error caused by data type conversion in the communication protocol. Fig. 6 shows the physical connection of the testing facilities. In this work, a controller prototype is designed based on the Raspberry Pi. The Raspberry Pi 3 Model B+ is a single board computer based on a 1.4 GHz, 64-bit quad-core processor boasting Ethernet interface. It is widely used in the field of the Internet of Things (IoT), automatic driving and machine vision due to the excellent computing performance (Garcia Guzman, Prieto Gonzalez, Pajares Redondo, Sanz Sanchez, & Boada, 2018). The real-time environment of the test bench is provided by “Simulink Desktop Real-Time”.

To compare with the designed nonlinear cooperative game (NC) controller, a linear cooperative game (LC) controller is designed. The LC controller consists of a linear MPC upper-level controller based on the approximate linearization of Eq. (13). Besides, the mean relative error (MRE) is utilized to evaluate the target tracking performances of the control methods.

$$\text{MRE}_v = \sqrt{\frac{1}{K} \sum_{k=1}^K |V_A(k) - V_{Des}(k)|^2} / \sqrt{\frac{1}{K} \sum_{k=1}^K |V_{Des}(k)|^2} \quad (60)$$

where \$V\_A\$ and \$V\_{Des}\$ denote the actual value and desired value of the vehicle state, respectively, \$v := \{\omega, \beta, v\_x, S\_{Lat}\}\$, \$K\$ is the number of samples.

The control parameters used in RT-HIL are shown in Table 3.

#### 5.2.1. Stuck-at-fixed-level fault

In this case, the test performances and fault type are the same as the numerical simulation.

Detailed plots of control performance in the stuck-at-fixed-level fault scenario are shown in Fig. 7. Fig. 7(a)–(c) indicate the vehicle yaw rate, side-slip angle and longitudinal velocity with or without control. One can be clear from these four figures that the vehicle states with

NC control can follow the reference values (RE) well even if actuator faults exist, and the control effects are preferable than LC. The vehicle trajectory is shown in Fig. 7(d), it is noted that the tracking error of vehicle trajectory under NC control is slightly larger than that under LC control at 150 m, but this difference is quickly corrected at around 180 m. Fig. 7(e) shows the tire utilization rate under NC control which maximum value is maintained near 1. Fig. 7(f) shows the MRE of the four control channels. It can be seen that the MRE of the longitudinal velocity and the lateral displacement under the two control methods are small. The vehicle yaw rate and the side-slip angle under NC control are improved by 0.15 and 0.91 compared with LC.

The outputs of AFS steering angle and in-wheel motor torques with NC control are shown in Fig. 8(a) and (b). It can be seen that the torques of the healthy motors exist a decline when the fault occurs to offset the additional torque caused by the stuck-at-fixed-level fault of the \$rl\$ wheel. The comparison of the controller virtual signal and the actual output of the steering motor in the HIL test platform is shown in Fig. 8(c). It obviously demonstrates the accuracy, real-time and practicality of the control algorithm.

#### 5.2.2. Additive fault

In this scenario, the vehicle suffering the additive fault is controlled to make a J-turn maneuver on a low friction surface with \$\mu = 0.4\$, and the vehicle longitudinal velocity is increased from 20 km/h to about 85 km/h in the 20 s. At 3 s, a torque of 250 N m is added to the \$rl\$ in-wheel motor.

The vehicle yaw rate is plotted in Fig. 9(a), which indicates the yaw rate of the controlled faulty vehicle can follow the reference well, whereas one without control jumps and deviates from the desired value. It can be concluded from Fig. 9(a) that the NC control not only has superior results but also faster responses than LC control. This advantage is especially noticeable after 10 s. A similar conclusion can be also drawn from the side-slip angle as shown in Fig. 9(b). The longitudinal velocity of the vehicle is illustrated in Fig. 9(c). Note that both two control methods can make the controlled vehicle to follow the reference well, but the LC control is closer to the reference value than that of the NC one. This is because NC control prioritizes stability compared to the

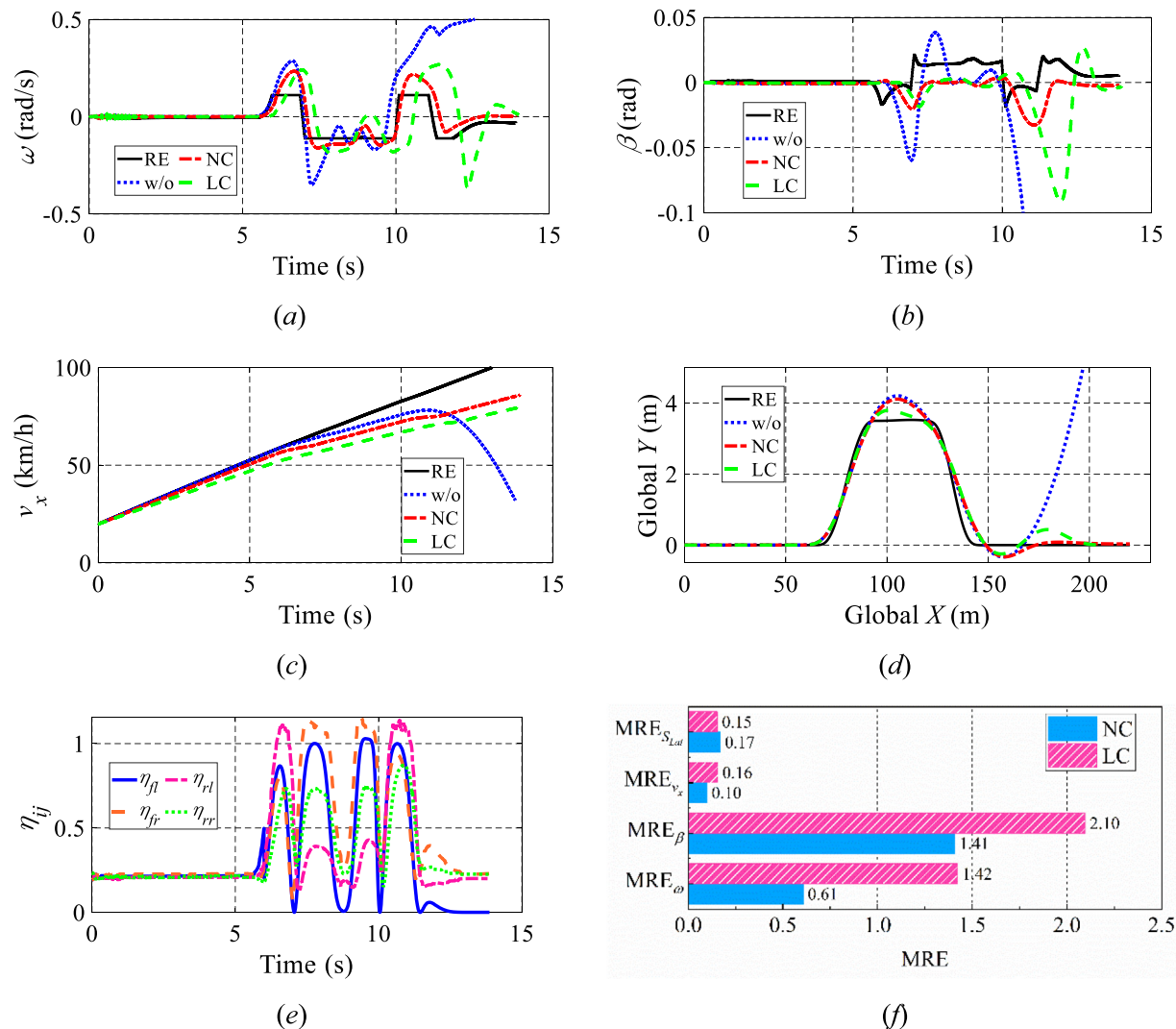


Fig. 11. Control results in the loss-of-effectiveness fault case. (a) Yaw rate. (b) Side-slip angle. (c) Longitudinal velocity. (d) Trajectory. (e) Tire utilization rate. (f) MRE.

power performance of the vehicle. Analyze the trajectory as shown in Fig. 9(d) can also serve as drawn a similar conclusion with Fig. 9(a) and (b). Fig. 9(e) shows the peak of tire utilization rate is maintained near 1. It can be seen from Fig. 9(f) that the longitudinal velocity and the lateral displacement under the two control methods can follow the target well. The vehicle yaw rate and the side-slip angle under NC control are improved by 0.37 and 0.91 compared with LC.

The actuator outputs of AFS steering angle and motor torques are shown in Fig. 10(a) and (b). It can be clearly seen that the torques of healthy motor exist a significant decline to offset the additional torque as soon as the additive fault of the *rl* in-wheel motor is introduced. The comparison of the controller virtual signal and the actual output of the steering motor in the RT-HIL test platform is shown in Fig. 10(c). It can be seen that the actual steering angle can be matched with the virtual signal not only numerically but also in real-time.

### 5.2.3. Loss-of-effectiveness fault

In this case, a loss-of-effectiveness fault that makes the torque of the *fl* in-wheel motor loss all of the control effectiveness is involved at 6 s of the vehicle during DLC. The road adhesion coefficient is chosen as 0.4 and the vehicle longitudinal velocity is increased from 20 km/h to 100 km/h in the 13 s.

Fig. 11(a) shows the yaw rate of the controlled vehicle can follow the desired value, even if the one without FTC seriously deviates from

the reference value due to the loss-of-effectiveness fault. Compared to LC control, the performance of the vehicle under NC control is closer to the reference value whether it is power performance or stability. Similar conclusions can be made from the vehicle side-slip angle, longitudinal velocity and trajectory, which are plotted in Fig. 11(b), (c) and (d), respectively. If the control strategy can handle the actuator occurs complete loss-of-effectiveness, the controller will also work well where the effectiveness of the actuator is partially lost. Fig. 11(e) shows that the tire utilization rate meets the control target. It can be seen from Fig. 11(f) that the vehicle yaw rate and the side-slip angle under NC control are improved by 0.82 and 0.69 compared with LC.

The signal outputs from the controller prototype under NC control are shown in Fig. 12(a) and (b). To display the NC control feasibility and real-time performance, the comparison of the virtual command from the HIL platform and the actual steering angle of the SBW system are plotted in Fig. 12(c). It can be observed that the steering motor can follow the control signal very well.

## 6. Conclusions

The main objective of this work is to establish an interaction mechanism among subsystems in the actuator fail case based on the cooperative game theory while considering the nonlinear characteristics of the system. A double-layer hierarchical controller is proposed to realize

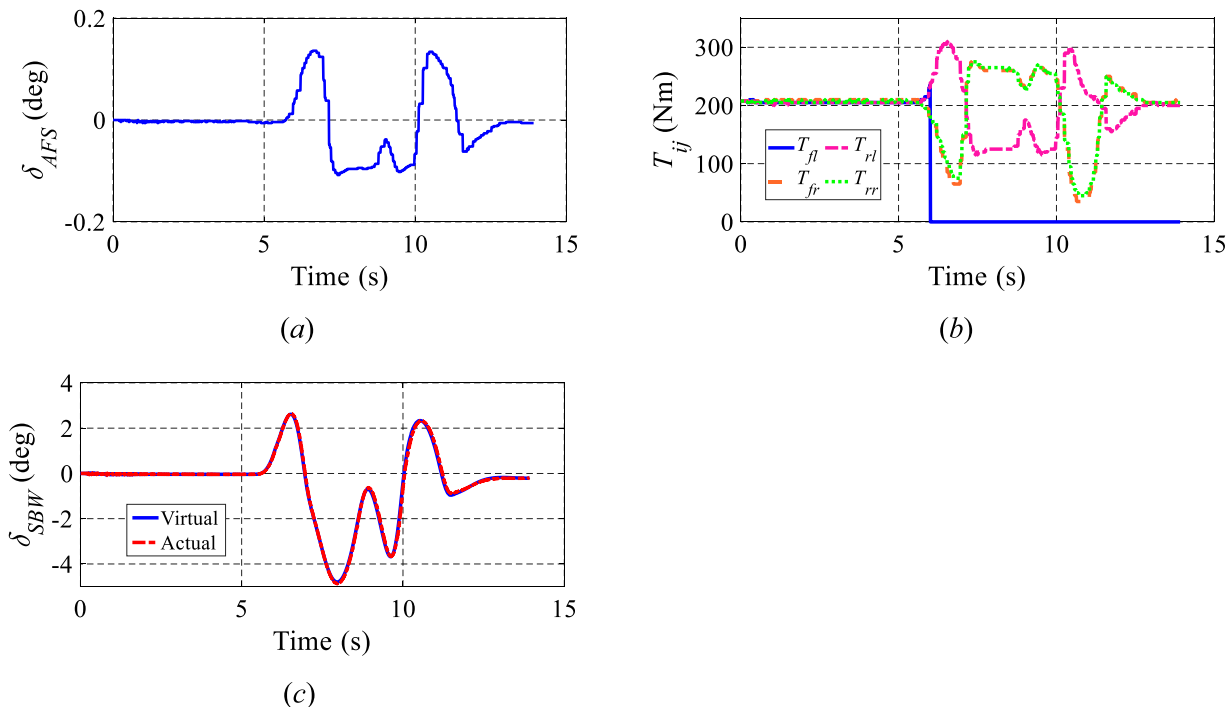


**Fig. 12.** NC controller outputs in the loss-of-effectiveness fault case. (a) AFS steering angle. (b) In-wheel motor torques. (c) SBW steering angle.

stability control of the 4WID-EVs with SBW under three types of in-wheel motor faults and driver in the loop. The main features of the proposed controller are as follows:

1. The input-output feedback linearization method is employed to deal with the nonlinear characteristic of the MIMO system.
2. The targets and actions interaction model among different actuators is established based on the DMPC-based cooperative game theory.
3. The analytical solutions of the cooperative game are obtained based on the QR and convex iterative method, which reduces the calculation complexity and is convenient for practical application.

The numerical simulation is performed to illustrate the difference between the cooperative game and noncooperative game in coordination. The results show that although the cooperative game and non-cooperative game have similar and satisfactory results, the cooperative game is more reasonable for task allocation.

Finally, the results of the RT-HIL test show that the proposed nonlinear method can improve the yaw rate and the side-slip angle by 14~82% and 69~91%, respectively. Therefore, the developed control method can guarantee the stability of the vehicle when any one of the three types of faults happens under different conditions.

In addition, there are still some issues waiting to be explored in future work. The driver's responses to the actuator fault are the important factors of vehicle stability. The information interaction framework in the cooperative game can facilitate the consideration of the driver's behavior in the FTC. Therefore, it makes sense to model the driver and the actuators as players in the game to study the interaction mechanism of them. Besides, the acquisition of more reasonable players' task weights is also worth studying.

#### Declaration of competing interest

The authors declare that they have no known competing financial interests or personal relationships that could have appeared to influence the work reported in this paper.

#### Acknowledgments

The work was jointly supported by the National Natural Science Foundation of China (Grant No. 51675066, 51005256), Chongqing Research Program of Basic Research and Frontier Technology (Grant No. cstc2017jcyjAX0323).

#### References

- Ataei, M., Khajepour, A., & Jeon, S. (2018). A novel reconfigurable integrated vehicle stability control with omni actuation systems. *IEEE Transactions on Vehicular Technology*, 67(4), 2945–2957. <http://dx.doi.org/10.1109/TVT.2017.2782569>.
- Chen, T., Chen, L., Xu, X., Cai, Y., Jiang, H., & Sun, X. (2019). Passive actuator-fault-tolerant path following control of autonomous ground electric vehicle with in-wheel motors. *Advances in Engineering Software*, 134, 22–30. <http://dx.doi.org/10.1016/j.advengsoft.2019.05.003>.
- Chen, Z., Zhang, B., Chen, B., & Fu, J. (2019). Development and evaluation of torque distribution methods for four-wheel independent-drive electric vehicle based on parameter estimation. *Advances in Mechanical Engineering*, 11(5), <http://dx.doi.org/10.1177/1687814019847405>.
- Erlien, S. M., Fujita, S., & Gerdes, J. C. (2016). Shared steering control using safe envelopes for obstacle avoidance and vehicle stability. *IEEE Transactions on Intelligent Transportation Systems*, 17(2), 441–451. <http://dx.doi.org/10.1109/TITS.2015.2453404>.
- Garcia Guzman, J., Prieto Gonzalez, L., Pajares Redondo, J., Sanz Sanchez, S., & Boada, B. L. (2018). Design of low-cost vehicle roll angle estimator based on Kalman filters and an IoT architecture. *Sensors (Basel)*, 18(6), 1800. <http://dx.doi.org/10.3390/s18061800>.
- Guo, B., & Chen, Y. (2019). Robust adaptive fault tolerant control of four wheel independently actuated electric vehicles. *IEEE Transactions on Industrial Informatics*, 16(5), 2882–2894. <http://dx.doi.org/10.1109/TII.2018.2889292>.
- Hu, C., Wang, R., Yan, F., & Karimi, H. R. (2016). Robust composite nonlinear feedback path-following control for independently actuated autonomous vehicles with differential steering. *IEEE Transactions on Transportation Electrification*, 2(3), 312–321. <http://dx.doi.org/10.1109/TTE.2016.2538183>.
- Huang, C., Naghdy, F., & Du, H. (2019a). Fault tolerant sliding mode predictive control for uncertain steer-by-wire system. *IEEE Transactions on Cybernetics*, 49(1), 261–272. <http://dx.doi.org/10.1109/TCYB.2017.2771497>.
- Huang, C., Naghdy, F., & Du, H. (2019b). Sliding mode predictive tracking control for uncertain steer-by-wire system. *Control Engineering Practice*, 85, 194–205. <http://dx.doi.org/10.1016/j.conengprac.2018.12.010>.
- Isidori, A. (1995). *Nonlinear control systems*. New York: Springer Verlag.

- Ji, X., Liu, Y., He, X., Yang, K., Na, X., Lv, C., et al. (2018). Interactive control paradigm-based robust lateral stability controller design for autonomous automobile path tracking with uncertain disturbance: A dynamic game approach. *IEEE Transactions on Vehicular Technology*, 67(8), 6906–6920. <http://dx.doi.org/10.1109/TVT.2018.2834381>.
- Ji, X., Yang, K., Na, X., Lv, C., & Liu, Y. (2019). Shared steering torque control for lane change assistance: A stochastic game-theoretic approach. *IEEE Transactions on Industrial Electronics*, 66(4), 3093–3105. <http://dx.doi.org/10.1109/TIE.2018.2844784>.
- Joa, E., Yi, K., Sohn, K., & Bae, H. (2018). Four-wheel independent brake control to limit tire slip under unknown road conditions. *Control Engineering Practice*, 76, 79–95. <http://dx.doi.org/10.1016/j.conengprac.2018.04.001>.
- Liu, Y., Yu, S., Gao, B., & Chen, H. (2015). Receding horizon following control of wheeled mobile robots: A case study. In *2015 IEEE international conference on mechatronics and automation (ICMA)* (pp. 2571–2576). Beijing, China: IEEE. <http://dx.doi.org/10.1109/ICMA.2015.7237892>.
- Maestre, J. M., de la Pena, D. M., & Camacho, E. F. (2011). Distributed model predictive control based on a cooperative game. *Optimal Control Applications & Methods*, 32(2), 153–176. <http://dx.doi.org/10.1002/oca.940>.
- Mahmud, M. A., Pota, H. R., & Hossain, M. J. (2012). Full-order nonlinear observer-based excitation controller design for interconnected power systems via exact linearization approach. *International Journal of Electrical Power & Energy Systems*, 41(1), 54–62. <http://dx.doi.org/10.1016/j.ijepes.2012.03.007>.
- Mihaly, A., Gaspar, P., & Nemeth, B. (2017). Multiple fault-tolerant in-wheel vehicle control based on high-level control reconfiguration. *IFAC Papersonline*, 50(1), 8606–8611. <http://dx.doi.org/10.1016/j.ifacol.2017.08.1428>.
- Mirzaei, M., Alizadeh, G., Eslamian, M., & Azadi, S. (2008). An optimal approach to non-linear control of vehicle yaw dynamics. *Proceedings of the Institution of Mechanical Engineers Part I-Journal of Systems and Control Engineering*, 222(14), 217–229. <http://dx.doi.org/10.1243/09596518JSCE444>.
- Na, X., & Cole, D. J. (2013). Linear quadratic game and non-cooperative predictive methods for potential application to modelling driver-AFS interactive steering control. *Vehicle System Dynamics*, 51(2), 165–198. <http://dx.doi.org/10.1080/0423114.2012.715653>.
- Na, X., & Cole, D. J. (2015). Game-theoretic modeling of the steering interaction between a human driver and a vehicle collision avoidance controller. *IEEE Transactions on Human-Machine Systems*, 45(1), 25–38. <http://dx.doi.org/10.1109/THMS.2014.2363124>.
- Na, X., & Cole, D. J. (2019). Modelling of a human driver's interaction with vehicle automated steering using cooperative game theory. *IEEE/CAA Journal of Automatica Sinica*, 6(5), 1095–1107. <http://dx.doi.org/10.1109/JAS.2019.1911675>.
- Rawlings, J. B., & Mayne, D. Q. (2016). *Model predictive control: Theory and design* (2nd ed.). Madison: Nob Hill.
- Sakthivel, R., Mohanapriya, S., Ahn, C. K., & Selvaraj, P. (2018). State estimation and dissipative-based control design for vehicle lateral dynamics with probabilistic faults. *IEEE Transactions on Industrial Electronics*, 65(9), 7193–7201. <http://dx.doi.org/10.1109/TIE.2018.2793253>.
- Sakthivel, R., Mohanapriya, S., Kaviarasan, B., Ren, Y., & Anthoni, S. M. (2020). Non-fragile control design and state estimation for vehicle dynamics subject to input delay and actuator faults. *IET Control Theory & Applications*, 14(1), 134–144. <http://dx.doi.org/10.1049/iet-cta.2018.5967>.
- Schnelle, S., Wang, J. M., Su, H. J., & Jagacinski, R. (2017). A driver steering model with personalized desired path generation. *IEEE Transactions on Systems Man Cybernetics-Systems*, 47(1), 111–120. <http://dx.doi.org/10.1109/TSMC.2016.2529582>.
- Shankar, S. (1999). *Nonlinear systems: Analysis, stability, and control*. New York: Springer Science & Business Media.
- Shuai, Z., Zhang, H., Wang, J., Li, J., & Ouyang, M. (2014). Lateral motion control for four-wheel-independent-drive electric vehicles using optimal torque allocation and dynamic message priority scheduling. *Control Engineering Practice*, 24, 55–66. <http://dx.doi.org/10.1016/j.conengprac.2013.11.012>.
- Tamaddoni, S. H., Taheri, S., & Ahmadian, M. (2011). Optimal preview game theory approach to vehicle stability controller design. *Vehicle System Dynamics*, 49(12), 1967–1979. <http://dx.doi.org/10.1080/00423114.2011.565778>.
- Wang, Y., Gao, J., Li, K., & Chen, H. (2019). Integrated design of control allocation and triple-step control for over-actuated electric ground vehicles with actuator faults. *Journal of the Franklin Institute*, 357(5), 3150–3167. <http://dx.doi.org/10.1016/j.jfranklin.2019.07.035>.
- Wang, R., & Wang, J. (2011). Fault-tolerant control with active fault diagnosis for four-wheel independently driven electric ground vehicles. *IEEE Transactions on Vehicular Technology*, 60(9), 4276–4287. <http://dx.doi.org/10.1109/TVT.2011.2172822>.
- Wang, R., & Wang, J. (2013). Passive actuator fault-tolerant control for a class of overactuated nonlinear systems and applications to electric vehicles. *IEEE Transactions on Vehicular Technology*, 62(3), 972–985. <http://dx.doi.org/10.1109/TVT.2012.2232687>.
- Wang, Y., Yu, S., Yuan, J., & Chen, H. (2018). Fault-tolerant control of electric ground vehicles using a triple-step nonlinear approach. *IEEE/ASME Transactions on Mechatronics*, 23(4), 1775–1786. <http://dx.doi.org/10.1109/TMECH.2018.2837128>.
- Wang, J., Zhang, G., Wang, R., Schnelle, S. C., & Wang, J. (2017). A gain-scheduling driver assistance trajectory-following algorithm considering different driver steering characteristics. *IEEE Transactions on Intelligent Transportation Systems*, 18(5), 1097–1108. <http://dx.doi.org/10.1109/TITS.2016.2598792>.
- Wang, Y., Zong, C., Li, K., & Chen, H. (2019). Fault-tolerant control for in-wheel-motor-driven electric ground vehicles in discrete time. *Mechanical Systems and Signal Processing*, 121, 441–454. <http://dx.doi.org/10.1016/j.ymssp.2018.11.030>.
- Yang, W., Feng, P., & Zhang, J. (2017). A comprehensive active-steering control method for improvement of vehicle handling performance. *Proceedings of the Institution of Mechanical Engineers, Part K: Journal of Multi-body Dynamics*, 232(3), 413–425. <http://dx.doi.org/10.1177/1464419317740294>.
- Zhang, D., Liu, G. H., Zhou, H. W., & Zhao, W. X. (2018). Adaptive sliding mode fault-tolerant coordination control for four-wheel independently driven electric vehicles. *IEEE Transactions on Industrial Electronics*, 65(11), 9090–9100. <http://dx.doi.org/10.1109/TIE.2018.2798571>.
- Zhang, H., & Wang, J. (2016). Vehicle lateral dynamics control through AFS/DYC and robust gain-scheduling approach. *IEEE Transactions on Vehicular Technology*, 65(1), 489–494. <http://dx.doi.org/10.1109/TVT.2015.2391184>.
- Zhang, G., Zhang, H., Huang, X., Wang, J., Yu, H., & Graaf, R. (2016). Active fault-tolerant control for electric vehicles with independently driven rear in-wheel motors against certain actuator faults. *IEEE Transactions on Control Systems Technology*, 24(5), 1557–1572. <http://dx.doi.org/10.1109/TCST.2015.2501354>.
- Zhao, L., Lu, S., & Zhang, B. (2019). Game-based hierarchical cooperative control for electric vehicle lateral stability via active four-wheel steering and direct yaw-moment control. *Energies*, 12(17), 3339–3360. <http://dx.doi.org/10.3390/en12173339>.